Damage-based finite-element modelling of in-plane loaded masonry walls repaired with FRCM

Jean-Patrick Plassiard, Ibrahim Alachek, Olivier Plé

To cite this version:

Jean-Patrick Plassiard, Ibrahim Alachek, Olivier Plé. Damage-based finite-element modelling of in-plane loaded masonry walls repaired with FRCM. Computers & Structures, 2021, 254, pp.106481. 10.1016/j.compstruc.2021.106481 . hal-03413868

HAL Id: hal-03413868

https://hal.science/hal-03413868v1

Submitted on 2 Aug 2023

Version of Record: https://www.sciencedirect.com/science/article/pii/S0045794921000031
Manuscript_755bfaa6bc601a3d0240726ba33b2e02

DAMAGE-BASED FINITE-ELEMENT MODELLING OF IN-PLANE LOADED MASONRY WALLS REPAIRED WITH FRCM

Plassiard Jean-Patrick[1*], Alachek Ibrahim[1], Plé Olivier[1]

Université Savoie Mont Blanc, CNRS, LOCIE, 60 rue du lac Léman, 73000 Chambéry, France

***Correspondence:**
Corresponding Author
jean-patrick.plassiard@univ-smb.fr

Highlights

- FRCM including a stainless-steel grid is efficient in terms of strength and ductility
- Local repair with FRCM strips is sufficient to recover the initial wall strength
- A damage-plasticity constitutive law reproduces the masonry behaviour correctly
- The pushover test on unreinforced and repaired walls can be modelled adequately
- The effect of repair finite elements is triggered from the start of the repair phase

Abstract

An empirical study of masonry wall repair is presented in the current work. The textile reinforced mortar used for repair comprises a stainless-steel grid embedded in a cement matrix. This composite was applied locally and along the cracks, on a previously damaged unreinforced masonry wall. The repaired wall was then subjected to a pushover load until its maximal strength was reached. Results of the damaged and repaired configurations indicate that recovery, and even a gain of initial stiffness and strength, was achieved. Finite-element simulations of the unreinforced and repaired walls were then carried out with an innovative approach to the repair modelling. The main features of the experimental Unreinforced Masonry Wall were reproduced. Finally, simulations of the repaired wall were generated to assess the gain in strength for several degrees of wall damage. Using this model, the crack patterns were investigated and the effects of different repair configurations are discussed.

Keywords: Masonry Wall, TRM, Repair, FE Modelling, Damage mechanics, Repair modelling.

1 Introduction

During the past century, masonry walls were commonly used in building constructions thanks to their relatively low cost and easy assembly, among others features. Before the application of seismic standards in France, unreinforced masonry (URM) was used. The purpose of the mortar joints was to link the brick rows, so that only a horizontal joint was considered. Such structures would not be permitted in seismic regions today, as vertical joints and wall ties became mandatory in France ([1],[2]). But the legacy of URM still coexists with current masonry buildings and their retrofitting is required. Even if structural retrofitting is necessary, the refurbishment of these buildings is mainly governed by considerations regarding energy and comfort. However, recent studies have shown that opting for solely a thermal refurbishment can lead to economic loss when an earthquake makes the building structurally unsafe [3]. It would make more sense to take into account both thermal conditions and seismic zoning when deciding whether thermal, structural or both types of retrofitting are required [4]. In this sense, a multipurpose panel involving both insulation coating and reinforcement may represent an optimal solution. This can be achieved with a double layer of materials that can even offer fire resistance [5]. An all-in-one solution based on a silica aerogel may also be possible, even if the compromise between the gain in thermal insulation and in mechanical resistance represents an optimization that is difficult to achieve [6]. In the following, we focus on the structural aspect, considering that thermal insulation is provided by an extra coating, for example.

Many studies have been devoted to the retrofitting of masonry walls, involving various reinforcement configurations with different composite materials. Nevertheless, as pointed out elsewhere [7], only a few studies have focussed on damaged walls. However, this configuration may be of utmost importance, for example in order to retrieve the structural capacity of a damaged building after a seismic hazard. Recent works have been performed in which several configurations of masonries, as well as damage and repair configurations were tested ([8], [9], [10]). The composite can be applied in several manners, depending on the type of failure to be prevented. In order to ensure the shear capacity against an in-plane loading, a set-up in grid or cross layout [11], in X layout ([12], [13]) or with two or three vertical strips [14] was tested. Full coverage of the masonry surface is also possible ([15], [16]). In most of these studies, the strength of reinforced walls is compared with that of unreinforced configurations. Generally, the gain-of-strength ratio ranges from a factor of 2 to 4. Here, the objective of the current study was not to obtain such an efficiency, but to answer the following questions: Can shear strength in a strongly damaged wall be restored after a repair operation? Can local repair in the form of a seam along the cracks suffice to ensure this regain of strength? The reasoning behind this idea is that local repair might not be required to improve the wall strength two or three times, as with a full coverage, in order to ensure the compliance with seismic standards. Moreover, a local application would be less time consuming and less expensive.

Previously, Fibre Reinforced Polymers (FRP) were largely used as a retrofitting solution for civil engineering applications. However, FRP appear to be less applicable to masonry because of their poor bond efficiency on irregular surfaces. FRP may also not be recommendable for building structures because of the lack of vapour permeability and fire resistance of these organic composites [17]. Moreover, building refurbishment on occupied sites is becoming common practice, with inhabitants potentially exposed to health hazards. Therefore, Textile Reinforced Mortars (TRM) were developed ([18], [16], [19] and [20]), characterized by fibre rovings, most often embedded in a cement matrix. This composite has the advantage of being able to cope with all the problems outlined above and even presents strong chemical compatibility with the masonry substrates. There are various types of fibres such as carbon, polypropylene basalt, steel or glass, among others, but natural fibres such as aramid or hemp can also be used [21]. Ferrocement [22] and in particular stainless steel may be used, offering several benefits. It is easily applicable for in situ configurations and can be utilized in several techniques as a reinforcement material, not only for TRM solutions ([13], [21] and [23]). [24] used a stainless-steel grid embedded in a mortar matrix to test the in-situ behaviour of retrofitted masonry walls. The width of the steel mesh was 50 mm. A tightened mesh comprising steel cords was tested and applied on several substrates [25]. This configuration allows for a diffuse and progressive generation of cracks.

Based on the available studies, it appears that the use of Steel Reinforced Grout (SRG) composites to retrofit URM walls might be an efficient retrofitting technique for enhancing the global in-plane behaviour of the walls and for preventing crack generation and openings. Compared with other materials, SRG offers the convenience of having strong ductility and stress hardening. However, for the design of repaired masonry structures, the assessment of existing masonry structures, and the analysis of local acting mechanisms of the reinforcement strips or sheets, numerical modelling is required in order to understand the structural behaviour under various loading conditions.

Many researchers proposed different approaches for the numerical study of unreinforced and FRP, SRG and TRM strengthened masonry structures. The main problem in the development of accurate stress analyses for masonry structures is the definition and the use of suitable constitutive laws of the material that take into account the heterogeneity of the masonry material resulting from the composition of blocks connected together by mortar joints and possible grout and reinforcement. Generally, two different modelling approaches based on the coupling of elastoplasticity and continuum damage mechanics are adopted to model the behaviour of masonry elements depending on the level of accuracy and the simplicity desired: micro- and macro-modelling. Mortar joints, masonry units, composite and mortar/units or composite/masonry interfaces are considered separately in the detailed micro-modelling approach while bricks and mortar are assumed to be smeared into a uniform composite material with average properties in the macro-modelling technique ([26], [27], [28]). In particular, [27] modelled reinforced masonry under out-of-plane loading by means of two different approaches: a detailed micro-modelling and a discretized homogenization model. For both models, a concrete model with a Drucker-Prager yield surface was used to consider the non-linear properties of materials and a combination of truss and solid elements was used to model external reinforcement. Similar models, micro- and homogenized models, have been proposed by [29] to predict the behaviour of FRCM-reinforced masonry walls under diagonal compression. [30] proposed a detailed micro-model to investigate the in-plane and out-of-plane behaviour of masonry panels. Masonry was treated as a two-phase material in which the bricks and the mortar were modelled as a continuum and the contact between the bricks and mortar was modelled using interface elements. [31] proposed 2D detailed and simplified models to study the flexural behaviour of retrofitted and non-retrofitted masonry beam-like specimens. [32] modelled thin mortar URM using a combination of a plane stress element and an equivalent joint interface. [33] studied the load-transfer mechanism in the case of FRCM strengthening systems by means of a simplified spring model, where each component of the strengthening system, i.e. mortar, reinforcement, support and reinforcement/mortar interface, is modelled as a spring with linear or non-linear behaviour. Another simplified model based on a bisection procedure with two different laws for the fibre mortar interface has been proposed by [34]. [35] used macro modelling for the masonry and truss elements for the fibre material; their interfaces were modelled with bond-slip behaviour. A perfect bond was assumed at the masonry fibre material interface.

With the aim of reproducing the behaviour of masonry walls repaired using FRCM composite under real service conditions, a finite-element model based on a micro-modelling approach is presented in this paper. The proposed model takes advantage of an already implemented non-linear orthotropic damage law, proposed by the authors in [36], in the finite element Code Cast3M [37]. The constitutive law, originally proposed for modelling concrete structures, has interesting benefits that makes it suitable for modelling brittle materials, such as masonry. In particular, it offers an anisotropic description of the cracking in such a way that a completely different behaviour along the principal axes is represented, which allows the constitutive law to be easily transposed to consider significant behavioural characteristics of brittle material. In each direction, two independent damage parameters are assumed, one for compression and one for traction, allowing the crack closure effect to be adequately described. Another important advantage of this model is that it uses only measurable input data, such as elasticity coefficients, tensile and compressive strengths, fracture energies and strains at the peak of the uni-axial stress–strain experimental curves.

In this context, the objective of the present study is to contribute to current efforts aimed at increasing the knowledge and understanding of the behaviour of unreinforced and FRCM-repaired masonry structures. To meet this objective, this study presents experimental and numerical investigations on the mechanical behaviour of masonry walls repaired using a composite consisting of a Stainless-Steel Grid embedded in a cementitious matrix (called "SSGRM" in this paper). First, a preliminary experimental study devoted to investigating the composition and mechanical properties of the composite material and the behaviour of undamaged, damaged and repaired masonry walls is presented. The test on the walls was conducted in three phases: an initial damage phase with a pushover test [2]. This test corresponds to the true load configuration of masonry walls in real service conditions, where a constant vertical load was first applied, subsequently followed by a lateral displacement imposed on the top edge side of the wall until the desired damage state was reached. A repair phase was then implemented during which the composite was applied, followed by a curing period. Finally, the strength of the repaired wall was assessed with a new pushover test. Results regarding of the initial stiffness, shear strength and crack localization are discussed in detail. One particularity of the test conducted here is the maintenance of vertical load during the whole test, thus also during the repair phase. This was motivated by the fact that a real wall is still subjected to what is called "in situ stress", even during a repair phase. Based on the non-linear orthotropic damage model presented in [36], three-dimensional finite-elements models were developed to simulate the response of the unreinforced and repaired masonry wall. The FE modelling of the masonry was performed with solid finite elements for all types of materials (brick, joint, reinforced-concrete beams, SSGRM). The calibration of the different properties of materials such as bricks and mortar joints allowed for a good prediction of the experimental results with the unreinforced configuration, which was obtained from the two first phases of the pushover test. Then, the effect of the in-situ stress was analysed using the FE model developed in which the SSGRM is incorporated. For the sake of simplicity, the composite was considered to be applied on the whole surface, unlike in the experiment. However, this makes it possible to evaluate the strength gain offered by such a configuration. Moreover, the effect of partial damage of the wall on the repair efficiency is assessed.

2 Characteristics of Stainless-Steel Grid Reinforced Mortar

2.1 Material Properties

Textile reinforced mortar is made of a cement matrix combined with a stainless-steel grid. The matrix is a manufactured mortar intended for the repair of reinforced concrete structures. Its thixotropic properties allow the composite to be moulded even along a vertical orientation. According to the technical data sheet of the material, the tensile and the compression strengths are 7.5 MPa and 35 MPa after 28 days, respectively. The manufacturer indicates that the product is not sensitive to fire. The steel grid comprises monofilaments of 1 mm diameter. They consist of waves with a mesh size of 6 mm in both directions of the grid, so that the free spacing between the yarns corresponds to a square of 5 mm per side. Moreover, the grid is 2 mm thick. Tensile tests were performed on the grid in order to define its properties. Three tests were performed on specimens that were 10 cm wide and 50 cm long. The results were reproducible, from one test to another. Average values of 1150 kN/m for the initial stiffness and 80 kN/m for the tensile strength were derived from the tests [20]. Besides these characteristics, a strong ductile behaviour was exhibited by each sample, as the strain at failure was approximately 30%while the strength measured just before the failure occurred was still maintained at its maximal value.

2.2 Mechanical properties of the composite

The different phases of the composite creation involve the application of a first layer of mortar on the brick, approximately 3 mm thickness, in which the grid is embedded. Then a second layer of mortar of the same thickness covers the grid, before being pressed down with a trowel. Thus, the SSGRM composite is 6 mm thick, which corresponds to the minimum thickness recommended by the RILEM [38]. Properties such as tensile strength, bond shear strength, anchoring length and stiffness can be derived from tensile test or bond test proposed in [38] and [39]. Here, a "2 in 1" test was chosen in order to evaluate these characteristics in a single test. This test configuration was previously used to compare the behaviour of TRM made of a stainless-steel grid and carbon grids [40]. The composite is 1 m long for a width of 0.1 m. 0.5 m of the composite is moulded on an assembly of two bricks while the other part is allowed free in order to apply the tensile load during the test (Figure 1).

Figure 1: Test configuration for the SSGRM composite and development of the crack pattern in the specimen.

Here two samples, assumed to be identical, were tested. Their initial stiffness is equal to approximately 6500 kN/m. After linear behaviour until a load of almost 3 kN, a series of tensile cracks started developing in the free part of the composite. The delamination of the composite from the brick also occurred during this phase, making it difficult to define the stress-strain relationship of the composite. A strong nonlinearity with hardening developed until an ultimate load was reached, ranging from 6 kN to 8 kN. Then, the composite failed, by debonding from the support, which indicated that its tensile strength should be at least equal to the ultimate bond strength. The computed exploitation ratio ranged from 75 to 100%, but tests on additional samples are required to refine these results. The shear strength of the bond between the composite and the brick can also be estimated from the tensile load measured just before the composite was pulled out of the brick. The corresponding load was 6.45 kN for Test 1 in Figure 2. At the same time, the remaining composite still bound to the brick was approximately 5 cm long. Considering a parabolic distribution of the shear stresses in the bond along the loading direction, a value of $\tau_{max} = 1.9$ MPa can be derived for the bond shear strength.

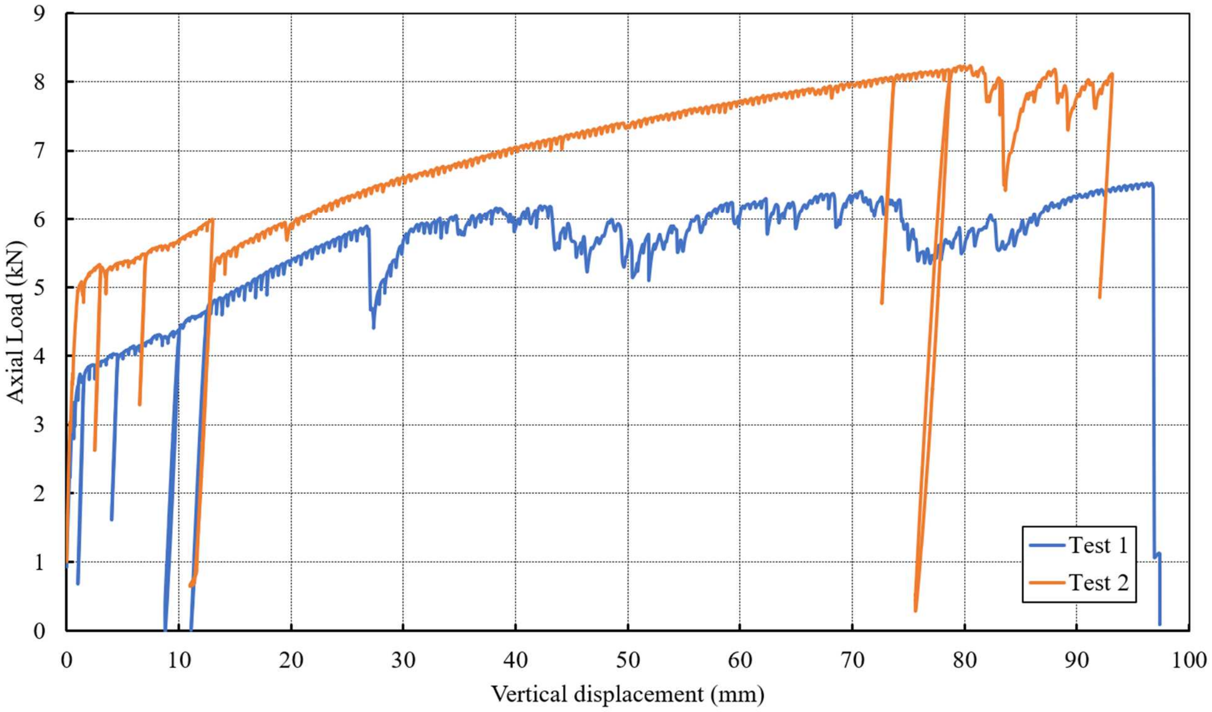

Figure 2: Force–displacement curve of the two SSGRM specimens.

Despite some dispersion in the results, the two tests showed similarities: linear behaviour followed by a strong ductility, diffuse cracks in the composite, hardening and debonding in the end. Further tests should be performed to identify the characteristics in more detail, but in this exploratory study, the results were considered sufficient in order to apply the composite as a repair solution for a damaged masonry wall.

3 Experiments at wall scale

3.1 Wall composition

The wall masonry tested is made of an assembly of hollow clay bricks. The bricks are 500 mm wide, 299 mm high and 200 mm thick. The brick holes are oriented in a vertical direction and represent 59% of the apparent brick volume. Compression tests conducted by the manufacturer on masonry wallettes showed an average compression strength of 8 MPa and a Young modulus of approximately1.5 GPa, in the direction perpendicular to the bed joints. The wall is 1.5 m high and 1.5 m long, corresponding to five rows of three bricks each. Joints between the bricks consist of a thin mortar joint that exhibited a tensile strength of 4 MPa and a compression strength of 14 MPa at 28 days. Here, only the horizontal joints were filled, in accordance with the masonry building topology from the period 1980-1990. The masonry wall was built on a reinforced concrete beam that made it possible to apply the boundary conditions during the experiment. For the same purpose, a second concrete beam was placed on the upper part of the masonry wall, through which the vertical load was applied to minimize local stresses and to obtain a uniform distribution of load during the test. These two beams and the masonry are also linked with a thin mortar layer.

3.2 Test configuration

The wall presented in section 3.1 was placed in a steel frame from which the boundary conditions can be applied. The steel frame is principally made of an assembly of HEB 400, which ensures the stability during the planned experiment. The wall was subjected to a pushover test, corresponding to an alternative to the more conventional cyclic loading such as in [7], [9] or [24]. Figure 3 shows the experimental set-up of this test. Recommended in the European standards [2], the common pushover test is performed in two loading steps: First, vertical loading is applied on the upper part of the wall and maintained constant after the target value is reached. Then, horizontal loading is applied to the top of the wall until failure of the masonry occurs, while the vertical loading is still active. Here, the vertical loading was applied by two load controlled electric actuators (EA1 and EA2 in Figure 3). A roller bearing system was placed on the top of the beam in order to release the horizontal constraint of the beam that would otherwise be generated by the contact between the beam and the actuators. The total vertical loading applied was 202 kN, which almost corresponds to the load encountered by a two-storey house, considering the dead and live loads [6]. The horizontal loading was applied by a hydraulic actuator (HA in Figure 3), from which 1-mm increments or decrements of displacement can be applied. The chosen rate was equal to 1 mm/min, so that quasistatic conditions were verified during the whole test. The lower beam required fixation in order to prevent any displacement of solid bodies while the loading was applied. In plane, the horizontal translation of the wall was prevented by a steel bar placed against the left part of the lower beam while the rotation was prevented by the vertical steel rods on the right part of the lower beam. Out-of-plane displacements were also prevented by four clamping fixtures placed along the lower beam. All of these displacement conditions were controlled during the test with displacement transducers. Moreover, two reinforced concrete beams were used to apply homogeneous loadings to the masonry, preventing the concentration of stress that would occurs with direct application of the loading to the masonry. The development of deformations and cracks in the masonry during the test was established with the use of digital correlation image (DIC) techniques. A high precision camera recorded images of the complete front surface of the wall every 5 seconds. Then, 7D software [41] was used to derive the appearance and growth of displacements, deformations and cracks. The precision of the camera combined with the capacity of the 7D software allowed for the detection of displacements and cracks of 20 µm, which facilitated tracking of the main displacements of the wall as well as the evolution of the cracks. During the test, regular control of the back side of the wall was also required to ensure that the cracks can be considered as uniforms in the out-of-plane direction.

The experiment was divided into three sequences. First, a pushover test was applied in order to generate damage in the wall. Then, the wall was repaired with the SSGRM composite under the applied vertical load. Finally, after 13 days of curing, the repaired wall was subjected to a pushover test again, until the failure of the wall was reached.

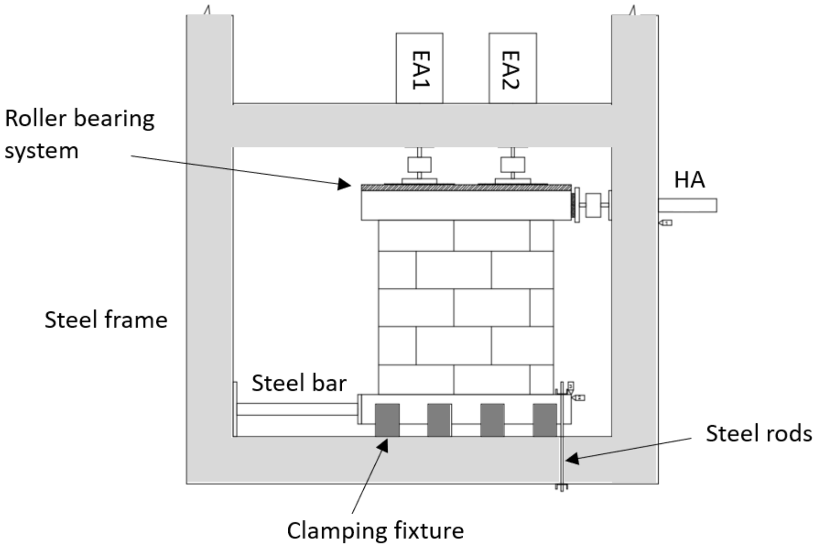

Figure 3: Pushover test configuration

3.3 Pushover test on the undamaged wall

The global shear behaviour of the wall was assessed with the force-displacement curve derived from the horizontal actuator measurement (Figure 4). The appearance of local cracks was deduced from the maximal shear strains provided by the 7D software, which correspond to the small images inserted along the curve. Here, dark blue denotes continuous deformation while a bright colour corresponds to a crack. It is worth noting that no scale was given for these colours, as this depends on the mesh size chosen for the DIC analysis, and also because a discontinuity (e.g. crack) is interpreted by the software as a strong continuous deformation. Thus, this information is purely qualitative.

A linear behaviour was observed up to a load of 60 kN, which corresponds to step 1. The corresponding stiffness is 15.3 kN/mm. No crack was noticeable at this stage. Then, a nonlinear behaviour developed until the maximum horizontal load of 75.8 kN was reached for a displacement of 7.4 mm. (step 2). Starting from the bottom, cracks developed along the first and second horizontal joints between the bricks. It should be noted that the vertical deformations between two bricks do not correspond to a crack here, as the vertical joints were not filled. On the other hand, a vertical crack was observed in the middle of the central brick in the bottom row. Then, we chose to increase the wall damage by continuing with the horizontal displacement. Instep 3, the load decreased to 73.2 kN for a displacement of 7.6 mm. The staircase failure (stepped crack pattern) was more pronounced with cracks reaching the third row of bricks. An inclined crack started to develop in the bottom left brick too. In step 4 (7.8 mm - 71.5 kN) the load still decreased, and the crack propagation was noticeable, starting from the bottom left brick and ending into the horizontal joint between the right brick in the second and third rows. Finally, a crack was also noticed along the joint between the rightmost brick in the bottom row and the lower concrete beam. These failure modes were interpreted as an intermediate case between flexural and staircase (shear) failure modes. This is also consistent with the results obtained by [42]. Then, the displacement was released until the load decreased to zero. During this phase, a cycle of loading – unloading was carried out to estimate the residual stiffness. A value of 13.6 kN/mm was deduced from the graph. After the load release, a residual displacement of approximately 2.5 mm remained in step 5. These relevant irreversibilities were concentrated in the failure path described in step 4. The strains derived from the DIC measurements indicate that the horizontal joints experienced shear strains while the vertical joints experienced tensile strains. The horizontal joints failed in mode II and then slipped. The vertical joints opened without cracking, since they correspond to dry joints. A similar crack pattern was observable on the back side of the wall. Finally, this failure mode and the corresponding value of maximal shear load were not expected for two reasons: previous experiments with identical walls and loading processes exhibited a staircase failure and a failure load of around 65 kN [6]. The corresponding walls and the one used for the current work were set up at the same time. One possible explanation may be given by the strengthening of the mortar joint caused by the longer curing period of the current wall, compared with the others.

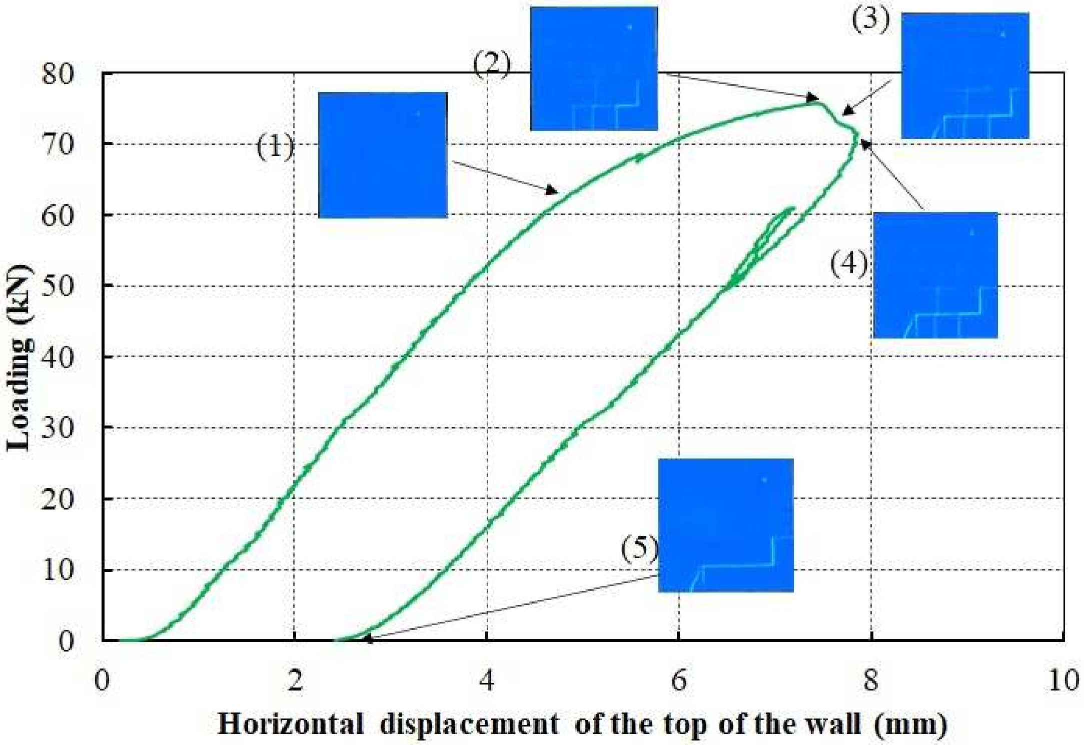

Figure 4: Experimental load–horizontal displacement curve at the top of the wall and evolution of cracks in the unreinforced wall

3.4 Repair sequence

After the damage phase, the repair sequence was undertaken. Based on the observation and the location of irreversibilities indicated in Figure 4, the location of the repair application was decided. In this work, the composite was voluntary applied in the zone located next to the cracks It works like a local seam along the cracks and is designed to renew the quality of the wall. Therefore, we did not attempt to strongly increase the wall capacity as previous studies did. Since no study of the required anchorage length had been undertaken in this work, it was decided to apply the SSGRM on a width equal to the brick height, corresponding to 15 cm on each side of the crack. The repair zone presented in Figure 5a was divided into several areas, to prevent any difficulties with the application caused by the hardening of the cement-based matrix. No overlapping of the composite was considered, assuming that it is not required for failure in mode I and that most of the stresses caused by a failure in mode II could also be transferred correctly. As presented earlier, the SSGRM was created in three steps: application of the first layer of mortar of approximately 3-mm thickness, application of the grid, application of the second layer of mortar slightly pressed down with a trowel. PVC plates of 6-mm thickness were used to delimit the repair area and to obtain the target thickness of the composite. The same method was used to repair the other side of the wall. Assuming that the cracks observed at the wall surface are representative of the cracks generated inside the wall, this application of the composite on both sides maintains the symmetry with respect to the out-of-plane direction. The repaired areas, after the curing period and the removal of the PVC plates, are shown in Figure 5b.

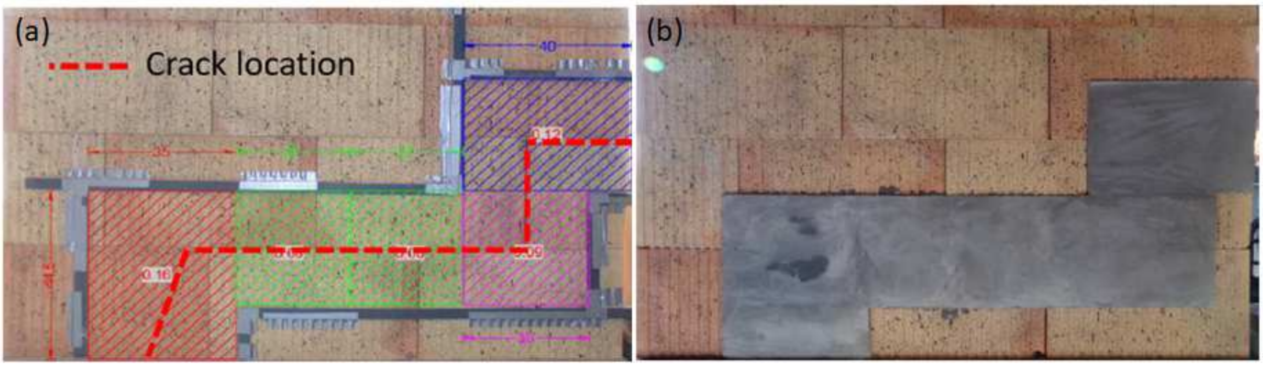

Figure 5: Repaired areas of the damaged masonry wall

The cure period applied for the composite was 13 days only, when conventionally it should last 28 days. This choice was made because of time restraints and will be discussed later. It is worth noting that the wall was kept in the metallic frame so that the vertical load of 202 kN was maintained on the wall during all of the repair period. This is quite different from previous studies, in which the repair or reinforcement of walls was realized on unloaded walls ([43], [14], [21], [7], [12] and [24]). This choice seems to be more in accordance with the in-situ configuration, when the gravity loads still act during the repair phase. The corresponding vertical stress is termed “in-situ stress” in the following. Two 1-cm thickness plates consisting of elastomers were placed between the actuators and the roller bearing system before phase 1. This allows one to lessen the decrease in loading by relaxation that could occur during the curing period. Daily control of the vertical loading indicated that the load reduction was less than 2% at the end of the curing period. Finally, maintaining the vertical load was also possible because the experimental study involved a single wall and not a series, as in the studies cited previously.

3.5 Pushover test on the repaired wall

After 13 days, the repaired wall was reloaded. First the vertical load was stabilized to the target value of 202 kN. Then, the lateral displacement was applied at a rate of 1 mm/min again. The relationship between the horizontal load and the horizontal displacement of the beam is presented in Figure 6. As for the undamaged wall, the maximal shear strain evolution derived from the DIC is presented for several key moments of the experiment. The behaviour was linear up to 55 kN, for a displacement of 2.95 mm. In this part, the stiffness is approximately 20.6 kN/mm and corresponds to an increase of 33%, compared with that of the undamaged wall. This can be explained by the stiffness regained for the damaged horizontal joints, and by the addition of stiffness along the vertical joints, which was not present for the undamaged wall. Several curves were noticeable in the range of 20–50 kN. They correspond to a series of unloading–reloading cycles intended to check the reversibility of the behaviour under moderate loading. Then, although the force – displacement curve exhibits a nonlinear relationship, no particular deformation was noticed until step 1, except that of the vertical opening of the composite in the middle of the central brick of the first row. This point corresponds to a displacement of 4.9 mm and a load of 76.4 kN, which is very similar to the maximal load reached for the undamaged wall. No change was noticed with the DIC analysis in the repaired area, while a crack zone was generated on the left part of the wall. This crack pattern continued to propagate until the maximal load of 83.2 kN was reached for a displacement of 7.5 mm (step 2). During this phase, several cracks appeared along the first crack, which extended to the top of the wall in a staircase pattern. The horizontal displacement was increased until a value of 9 mm (step 3), resulting in a reduction of the horizontal load to 78 kN. It was decided not to increase the displacement further because the crack crossed the wall from the bottom to the top. Moreover, corner crushing was starting to develop, and could result in a sudden loss of stability. Finally, the displacement was decreased until the horizontal load was totally released (step 4). The remaining displacement was approximately 1 mm. Crack reclosure, however, was not noticed with the DIC analysis. Moreover, the vertical crack initiated in the middle brick of the bottom row propagated along the repair zone. Finally, this was the only place where the repair area appeared to be damaged. Thus, the repair material and the curing time proved to be sufficient in this experiment.

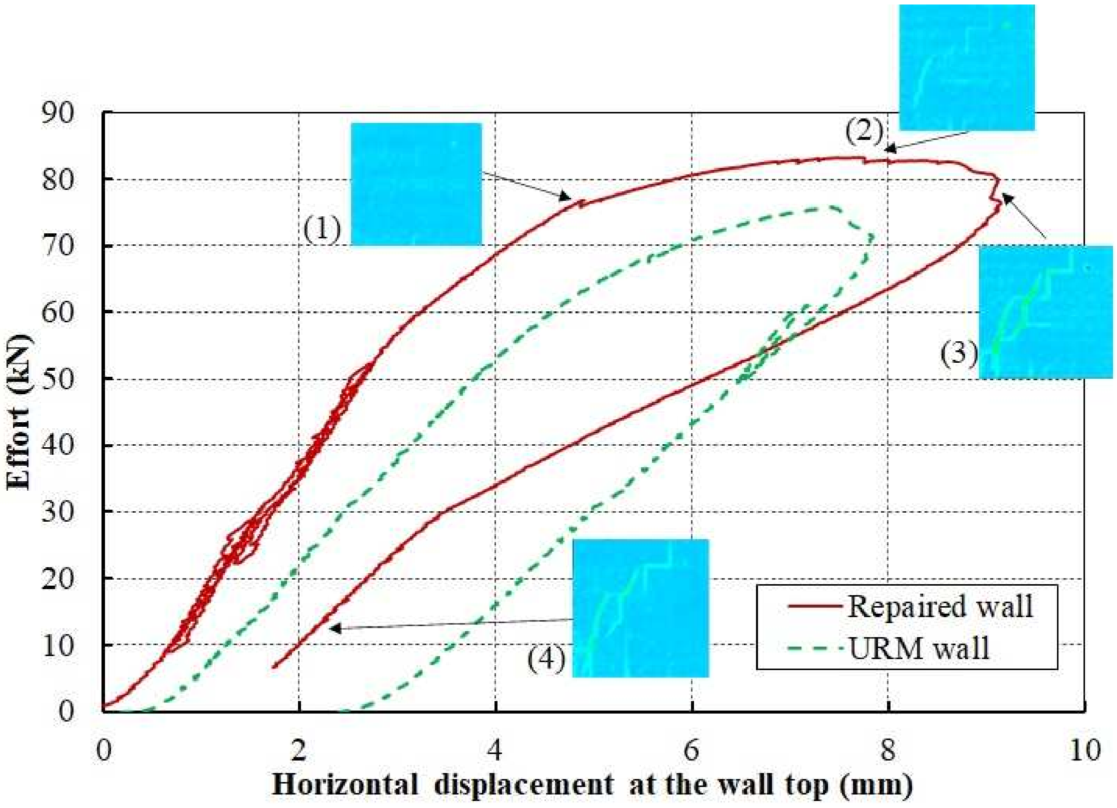

Figure 6: Comparison between the load–displacement curves of the unreinforced masonry wall (URM) and the repaired wall.

The behaviour of the repaired wall can be compared with the behaviour of the undamaged one. First, the crack pattern was different. The repair prevented the initial failure from occurring again. Thus, the failure was deflected out of this area and a higher maximal load was found when compared with the first loading. Previous studies have shown that the masonry retains a memory of the available strength. In other words, the strength of the damaged wall was approximately 71.5 kN before the repair phase, whereas after the repair phase, the strength increased to 83.2 kN, corresponding to a strength gain of 16%. This is far less than the gain of strength obtained in several studies ([7], [44], [9] and [24]). This low gain of strength can be explained by the local repair of cracks in the wall. A global repair could be applied here but a local application of the composite along the cracked areas was chosen to show the efficiency of this repair system. In conclusion, the experimental results here showed that the repair of the damaged area of the masonry wall using SSGRM allows more than the initial strength of the wall to be recovered, with low costs in terms of materials and execution.

4 Numerical modelling

4.1 Modelling strategy

The experiment carried out in this study has shown the potential of the SSGRM composite to renew and recover the strength capacity of a wall involving serious damage, even with a local repair. However, the test condition, by pushing the load further than the maximal load, is relatively more demanding, compared with walls subjected to 70% or 100% of the ultimate peak load [7]. Moreover, the SSGRM was applied locally, whereas a complete covering of the wall with the repair material is quite common in the literature. In order to compare the SSGRM with other composite solutions, a numerical model was developed. The micro-modelling approach of the finite-element method was used to model each component of the wall described above. This method was initially proposed by Lourenço for masonry [28]. Since then, this approach has been generalized to the study of unreinforced or reinforced masonry walls ([45], [46], infilled frames ([47] and [48]), vaults [49] or bridges [50]).

As pointed out in [26], several levels of micro-modelling were proposed for the joints, depending on how the joints between the brick are modelled (modelling of the mortar and its interface with the bricks separately or not). If the mortar and the mortar-brick interfaces are modelled together in a single element, then the numerical approach is named “simplified micro-modelling”. In this case, interface elements are commonly used to model the interfaces in order to represent the discontinuity that may occur ([33], [32]). Several models using interface elements are capable of capturing mode I and mode II of cracks. The second approach considers the mortar as a continuous element and the interfaces as discontinuous elements. This last approach may be more precise, but a wide range of characterization tests are mandatory to define the mechanical properties adequately [30]. One main issue with this approach concerns the incorporation of an interface for the SSGMR. Indeed, numerical models tested during this study have shown that the contact conditions between interfaces along three directions make the convergence of the simulation difficult to obtain. To overcome this difficulty, an alternative approach is proposed in this work, by modelling the mortar layer as a single element. It was already used to model experiments with confined masonry walls from [51]. Instead of a discontinuous element, the mortar unit was modelled with a thin solid element, for horizontal and vertical joints. Furthermore, to model the cracks observed in the units during the experimental test in the upper and lower rows, vertical joints with 1-mm thickness were modelled in the middle of each unit of brick. For this reason, the mesh consistency requires that the middle part of the brick is made of the same small elements as the adjacent joints (Figure 7). As a result, each complete brick is made of two halves of brick and a thin vertical layer of element between them. In this way, a vertical weakness is created inside the brick, as in [52]. Here, the failure is also possible in the whole brick thanks to the damage constitutive law used. Several issues were addressed with this modelling strategy. First, the sizes of the bricks and mortar were equal to those in real settings, unlike when interfaces with virtual thickness are used. Nevertheless, this should have only a minor effect here, as the mortar joints are thick compared with the brick size.

Furthermore, considering the SSGRM composite, it could be modelled as a homogeneous material that fails in tension by exhibiting strong ductility. On the other hand, the interface between the SSGRM and the brick shows shear failure with a brittle behaviour. The constitutive law available in the software used does not allow such a range of behaviours to be modelled. For example, the formulations of Mohr–Coulomb or Drucker–Prager do not incorporate a possible softening in shear behaviour, making the model unable to capture the correct failure mode of the masonry wall [6]. Moreover, the debonding between the masonry substrate and the cementitious mortar of the SSGRM is less likely to occur in this type of repair system [53]. This was confirmed in the experimental test where no visible crack or debonding areas were noticed at the composite–masonry interface. For these reasons, the debonding at the masonry–SSGRM interface is not introduced in the present model and a perfect bond between masonry and composite layers was assumed.

Finally, another main issue concerns the modelling of the repair operation. Unlike the retrofitting operation that was performed on a healthy structure, in the repair of structures, the composite material is applied on damaged or deformed elements. Numerically, the simulation of the repair process involves the insertion of finite elements on the deformed mesh, which could be hard to achieve. Another way of modelling this phase of repair is to model the repair element (i.e. finite element used to create the SSGRM mesh) with the different elements of the structure from the beginning but with a non-solidified matrix in the initial phase of loading and with a completely solidified matrix, which means that a new material parameter must be introduced to take into consideration the state of the repair elements (active or not). This is the method that was applied in the current study using the orthotropic damage constitutive law presented in [54]. Recent developments have been made in this law to incorporate the effect of creep, temperature, drying and hydration [55]. In their model, the authors introduced a degree of hydration to represent the fraction of material that is able to support stress. This hydration degree ranges from 0 for a non-solidified matrix to 1 for a completely solidified matrix. It is with this hydration behaviour that the delayed effect of the repair material was carried out. During the first damage phase, no hydration of the material is considered, so that finite elements representing the repair are not constrained and do not influence the behaviour of the rest of the wall. Then, at the very beginning of the second phase, hydration is applied so that the SSGRM model is able to generate resistance during the second loading phase. The consistency of this approach was verified by comparing the loading curve obtained during the first phase for both the model of the URM wall and the model incorporating the SSGRM. These two models showed very similar results during the first phase.

Finally, all the materials were modelled with the orthotropic damage constitutive law introduced in the next section, except for the concrete beams and the loading plate for which an elastic model was used. It is worth noting that we do not claim the model presented below respects the concept of unicity of the parameter set. Such an approach requires several characterization tests that were not been undertaken here, for example compression and tensile tests on the brick, shear tests of the joints. Nevertheless, it will be shown that the main features of the behaviour can be reproduced by using the usual parameters.

4.2 Presentation of the constitutive law

In this section, the main parameters required for the calibration of the model are presented. More explanations as well as application types can be found in [56] and [54]. The total stress tensor σ_{ij} is computed from the effective stress tensor $\tilde{\sigma}_{kl}$, using Eq. 1. This tensor is divided into a positive part $\tilde{\sigma}_{kl}^{+}$ for the tensile stresses and into a negative part $\tilde{\sigma}_{kl}^{-}$ for the compression stresses. In this formulation, four damage types are considered. The pre-peak damage in tension is isotropic and is denoted by D_0^t. It occurs if the pre-peak behaviour is not linearly elastic. Then, orthotropic damage in tension D^t enters in the post-peak phase, corresponding to the localization of the tensile crack. The value of D^t depends on the fracture energy in tension G_{FT}. The size of the finite elements is also required, in order to prevent the effects of mesh dependency [57]. The shear compression damage D^S is isotropic and is driven by the plastic dilatancy and a characteristic dilatancy threshold $\varepsilon_{k,s}$. A high value of $\varepsilon_{k,s}$ corresponds to brittle behaviour in shear, while a low value corresponds to ductile behaviour. Finally, a damage variable D^r is also considered for the reclosure of tensile cracks, if compression stress is applied at a later stage. Depending on the compression stress applied, the stiffness is partly or totally recovered. The corresponding damage value D^r is derived from the re-closing energy G_{FR} required to reclose the crack and from the corresponding compression stress value R_R.

$$\sigma_{ij} = (1 - D^S)\left[(1 - D_0^t)(1 - D^t)_{ijkl}\,\tilde{\sigma}_{kl}^{+} + (1 - D^r)_{ijkl}\,\tilde{\sigma}_{kl}^{-}\right] \qquad (1)$$

Hooke's law is then considered for the elastic behaviour of the effective stresses. The effective stress tensor $\tilde{\sigma}_{kl}$ depends on the elastic strains ε_{kl}^{e} (Eq. 2) and on the tensor of elasticity C, where C is a function of the elasticity modulus E and the Poisson ratio υ:

$$\tilde{\sigma}_{ij} = C_{ijkl}\,\varepsilon_{kl}^{e} \qquad (2)$$

The plasticity is controlled with two plastic criteria. A Rankine criterion f^t monitors the appearance of inelastic strains in the direction of the major tensile stress as soon as the uniaxial tensile strength R_T is reached. The compression–shear plasticity is described with a Drucker–Prager criterion f^{DP} for which two parameters have to be considered: the uniaxial compression strength R_C of the material and the Drucker–Prager confinement coefficient δ, calculated using Eq. 3 This last parameter controls the effect of the confining stress on the strength and depends on the internal friction angle ϕ of the material as follows:

$$\delta = \frac{2\sqrt{3}\,sin\phi}{3 - sin\phi} \qquad (3)$$

The plastic flow in tensile behaviour is associated, and thus no extra parameter is required. On the other hand, the plastic flow in shear behaviour is non-associated. It is handled by the dilatancy coefficient β, and a characteristic strain $\varepsilon_{k,s}$, that controls the post-peak behaviour in shear. A low value of $\varepsilon_{k,s}$ results in brittle behaviour while a high value induces ductile behaviour after the peak. The last aspect that is considered here is related to the solidification of the material. It is ruled by the hydration degree ζ, which ranges from 0 for a non-resistant material to 1 for complete solidification.

4.3 Presentation of the model

For the numerical study, the modelling of two types of walls was considered. Figure 7 presents the URM wall, considering the masonry, the upper and lower concrete beams and the metallic plate on which the horizontal loading is applied. A 3D-FE mesh of the wall was generated using the CAST3M software [37]. The masonry corresponds to the bricks, the vertical dry joints and the horizontal mortar joints, which are also shown in Figure 7. The wall with the SSGRM composite is presented in Figure 8. This is the same model as the URM wall, except that elements to model the SSGRM were added on each side of the masonry. For the sake of simplicity, the cement matrix and the stainless-steel grid are modelled as a single homogenized material. In the model, the SSGRM covers the whole surface of the masonry, but here it was partially omitted to allow for the distinction of the different layers. Along the out-of-plane direction, the SSGRM is divided into three layers of elements of the same thickness, as shown in Figure 8. In particular, the layer of element located against the wall aims to reproduce the damage or cracks that may occur at the masonry-SSGRM interface. These elements belong to what is called the “SSGRM interface” while the other two layers of elements are identified as the “SSGRM core”. In summary, the elements of the SSGRM interface have the same properties in tension as the elements of the SSGRM core, but the SSGRM interface display a different behaviour in shear compared with that of the SSGRM core.

Only solid parallelepiped elements (CUB8: massif 8-node cubic elements) are used in the whole model, including the concrete beams, the metallic plate, the vertical and horizontal joints, the SSGRM and finally the half of bricks and thin vertical layer of bricks discussed earlier. For this reason, the geometry of the numerical model almost corresponds to the experimental one. The only difference concerns the length of the bricks that have to be decreased by 1 mm, to compensate for the thickness of the vertical dry joints.

Each brick half is represented with eight elements in length and height, while six elements are considered for the thickness direction. Mortar joints and dry joint correspond to a single element in thickness, while the other dimensions are conditioned by the brick elements. As presented above, three elements in thickness direction are considered for the SSGRM modelling, while the element size in other directions is controlled by the masonry modelling. It is worth noting that the symmetry of the problem could have been used to model only half of the geometry, but the aim of addressing unsymmetrical configurations in the near future favoured the choice of full modelling.

Finally, 20,868 elements were involved in the model of the unreinforced wall versus 37,536 for the repaired wall. Boundary conditions involve the pinning of all elements on the bottom face of the bed beam. A uniform vertical stress is applied progressively on the upper surface of the upper beam until the desired force of 202 kN is achieved. This load is then kept constant during the rest of the simulation. After the vertical loading reaches its target value, an increment of displacement is imposed in the required step in order to reproduce a similar horizontal displacement than the one applied during the experiments. The pushover loading is achieved by imposing a target evolution of the horizontal displacement of the node located in the centre of the metallic plate. The total amount of displacement was divided into a number of sub-steps in the FE analysis. The CAST3M software uses the Newton–Raphson iterative method to provide convergence at the end of each load increment within a tolerance limit. In this study, the convergence criterion was based on displacement, and the convergence tolerance limit was initially selected and fixed at 10^{-4}. It is worth noting that only the horizontal displacement of the node is prescribed here, so that any buckling failure is free to develop, as for the experimental case.

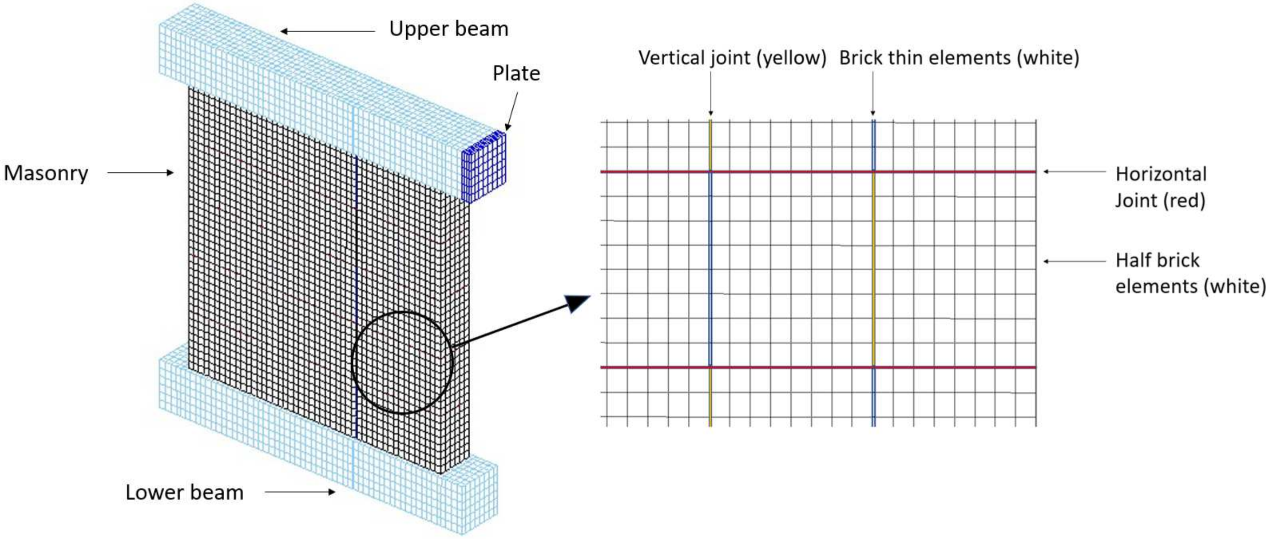

Figure 7: Numerical configuration for the URM wall and front view of the masonry modelling.

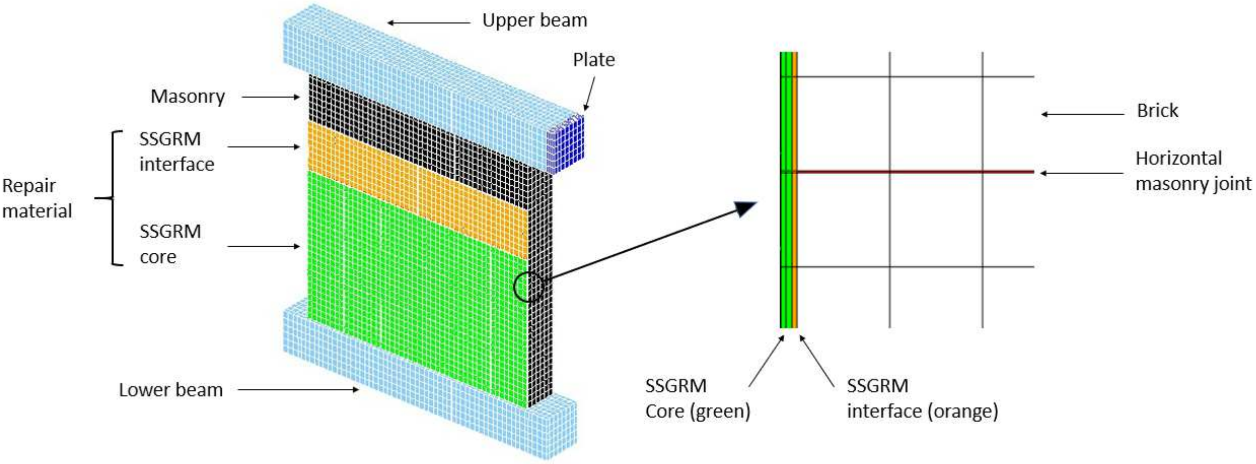

Figure 8: Numerical configuration for the wall with repair material and side view of the SSGRM modelling.

The concrete beams and the steel plate were considered as linear elastic materials with the usual properties of steel and concrete. Young's modulus E was set to 30 GPa for the beams and to 210 GPa for the metallic plate. Both Poisson ratios υ were set to the default value of 0.2. The constitutive law, described in section 4.2, was used for the bricks, dry and mortar joints and SSGRM repair materials. The parameters chosen for the masonry part of the model are presented in Table 1. The value retained for Young's modulus E of the horizontal joints was taken from [6]. Vertical joints are dry, and therefore their Young modulus was considered equal to that of the brick. Finally, the value for the brick was set to reproduce the initial stiffness of the experimental first loading of the wall. This calibration is mandatory, because of the brick anisotropy. Poisson's ratio υ was set to a standard value of 0.2. Some parameters, such as the compression strengths R_C of the bricks and of the mortar joints, were deduced from previous characterization tests, but most of the other parameters were estimated. This is the case for the tensile strengths R_T of the bricks and mortar joints. It is worth noting that a higher tensile strength is considered for the top and bottom horizontal joints. Indeed, the contact surface between these joints and the beams is higher than between two bricks, so that a better resistance can be offered. They correspond to the first value of tensile strength in Table 1, while the second value corresponds to that of the brick-to-brick joints. Other parameters suck as the strains at peak ε_{PT} in tension and in compression ε_{PC} were set at a default value, corresponding to a linear elastic behaviour before the peak. Values for the fracture energy in tension G_{FT} and for the crack reclosure energy G_{FR} are expressed as a function of the previous parameters. Their values are established in relation with the ones given in [56], as well as for the reclosure characteristic stress R_R . A Drucker–Prager confinement coefficient δ of 1.0 was considered for each type of joint, while a value of 0.6 was set for the bricks. The dilatancy was assumed to be negligible in the first approach for all materials, except for the brick, whose dilatancy coefficient β was set to 5.10^{-2}.

The interface and the core parts of the composite were calibrated so that their association is similar to the three stages observed during the experimental tensile tests: a linear behaviour followed by a hardening stage with a strong ductility, and finally, the debonding of the interface. In this study, the tensile behaviour was approximated with an “elastic, perfectly plastic” approach. First, Poisson’s ratio is set to 0.2, as for the other materials. As observed during the characterization tests on the composite, the initial stiffness is almost equal to 6500 kN/m, while the ultimate load is approximately 7 kN. Considering the dimension of the composite, it corresponds to a Young modulus of 5400 MPa and a tensile stress of 11.6 MPa. No damage was considered before the peak, so that the strain at peak ε_{PT} is defined by the previous parameters. Then, the strong ductility is reproduced with the use of a high value of fracture energy in tension G_{FT}. Compression and shear behaviours are considered next. The composite is glued on the external surface, so that no confining stress acts on it. Thus, the confinement coefficient δ was set to 0. The compression strength R_c was adjusted to obtain a shear failure for the value τ_{max} computed in section 2.2. As a consequence, the compression strength is roughly equal to a fourth of the tensile strength. This unusual observation should not affect the results as long as no failure in compression occurs in the SSGRM material. The characteristic strain $\varepsilon_{k,s}$ was set to a low value in the interface part of the SSGRM, to reproduce the brittle debonding observed in the experiment. On the other hand, a high value was attributed to this parameter for the SSGRM core, as no failure in shear was experienced inside the composite. Other parameters such as the dilatancy coefficient β, the reclosure characteristic stress R_R and the crack reclosure energy G_{FR} were set to their standard values.

The last parameter considered is the hydration advancement coefficient ζ. As a reminder, the material has a non-solidified behaviour if this parameter is set to 0.0, while complete solidification is obtained for ζ =1.0. Therefore, its value was set to 1.0 by default, apart from the composite for which two values were used (Table 1). A low value was applied during the phases in which its presence should not affect the behaviour of the masonry. Then, it is set to 1.0 just before the beginning of the reloading phase on the repair wall, in order to be assessed.

Table 1: Parameters set of materials for the simulation

Materials	Brick	Vertical joints	Horizontal joints	SSGRM interface	SSGRM core
Young’s modulus E (MPa)	600		5000	3250	
Poisson ratio ν (-)	0.2				
Tensile strength R_T (MPa)	1.0	10^{-3}	0.5 / 0.15	11.6	11.6

Strain at tension peak ε_{PT} (-)	$1.0 \times {}^{R_t}/_{E}$				
Fracture energy in tension G_{FT} (MJ/m^2)	$1.0 \times \varepsilon_t \times R_t$			$10^6 \times \varepsilon_t \times R_t$	
Compression strength R_C (MPa)	8.0	10^{-3}	10.0	3.3	3.3
Strain at compression peak ε_{PC} (-)	$1.0 \times {}^{R_c}/_{E}$				
Characteristic strain $\varepsilon_{k;s}$ (-)	10^{-5}	10^{-5}	10^{-5}	10^{-8}	10^{-3}
Drucker Prager coefficient δ (-)	0.6	1.0	1.0	0.0	0.0
Dilatancy β (-)	5.0×10^{-2}	10^{-3}			
Reclosure characteristic stress R_R (MPa)	$2.0 \times R_t$				
Crack reclosure energy G_{FR}	$1.0 \times G_{ft}$				
Hydration advancement ζ (-)	1.0	1.0	1.0	10^{-3} / 1.0	10^{-3} / 1.0

4.4 Validation of the finite-element model

The numerical load–displacement diagram of the URM is shown in Figure 9. The simulation of the URM wall is divided into two phases, while three phases are necessary for the repair wall. However, the first two phases are very similar for both walls. The first phase is dedicated to the progressive application of the vertical stress, which will be maintained as constant during the subsequent phases. Only 20 iterations are required to apply this loading phase. Then, the second phase corresponds to the first horizontal loading–unloading, which generates the wall damage. This horizontal loading is first composed of 300 displacement steps of 3.10^{-2} mm each, corresponding to a maximal displacement of 9 mm. For the sake of simplicity, it was chosen in the following to impose displacement increments of ± 3.10^{-2} mm only. The unloading is composed of negative incremental displacements of the same magnitude until the total release of the horizontal force. It is important to remember that during these first two phases, the SSGRM elements of the repaired wall are not "active", as the hydration advancement ζ is set to almost 0. The load–vs–displacement curve during phase 2 is presented in Figure 10 for both types of wall, the URM wall without an SSGRM element and the wall with inactivated repair elements. The two wall responses are very similar. This finding confirms that the effect of the SSGRM element is negligible during the first two phases.

According to the results obtained from the URM wall, linear behaviour occurs until a load of around 50–60 kN. Then, nonlinear behaviour starts to develop, until the maximal lateral strength of 76.67 kN is reached, for a horizontal displacement of 7.6 mm. This corresponds to a load difference of 1%, compared with the experimental value. After that, the load decreases slightly until a value of 74.5 kN is reached for the maximal displacement of 9 mm. Then, the unloading is built up with negative displacement increments of the same magnitude as during the loading part, until the horizontal load is completely released. As the behaviour is nonlinear, residual deformations of the masonry take place. This corresponds to a residual displacement of 0.4 mm in the horizontal direction, so that only 285 steps are required for the unloading part. Similar trends to the loading phase of the experimental curve are noticeable, such as linear behaviour or maximal strength. However, the maximal strength corresponds instead to a phase of plateau, while a load decrease was obtained for the higher displacements during the experiments. The deformed mesh of the wall for the maximal displacement is presented in Figure 11. In accordance with the experiment, the joints located on the right part of the two lower brick rows are strongly deformed (Figure 11). The cracks opening at this stage can also be derived from the plastic strains, as shown in Figure 11, where WPLO denotes the crack width in millimeters. A failure occurs in the bottom joint between the brick and the concrete beam. The failure is an intermediate case between the flexural and the shear modes, as is the case in the experiment. The main difference concerns the absence of cracks in the left and central bricks of the first row and of the joints around the last one. This may explain the presence of a plateau in the simulation while a decrease of the load was observed in the experiment. During the unloading phase, a strong decrease in the horizontal displacement occurs between 7 and 4 mm. This corresponds to the reclosure of most of the cracks, so that the residual displacement is almost one fourth of the experimental displacement. This first simulation indicates that it is possible to reproduce the main features of the URM wall such as lateral strength and failure mode by using the usual parameters. Certainly, this finding needs to be confirmed with several modelling studies of URM walls, but it emphasizes the significance of micro-modelling with solid elements for joints.

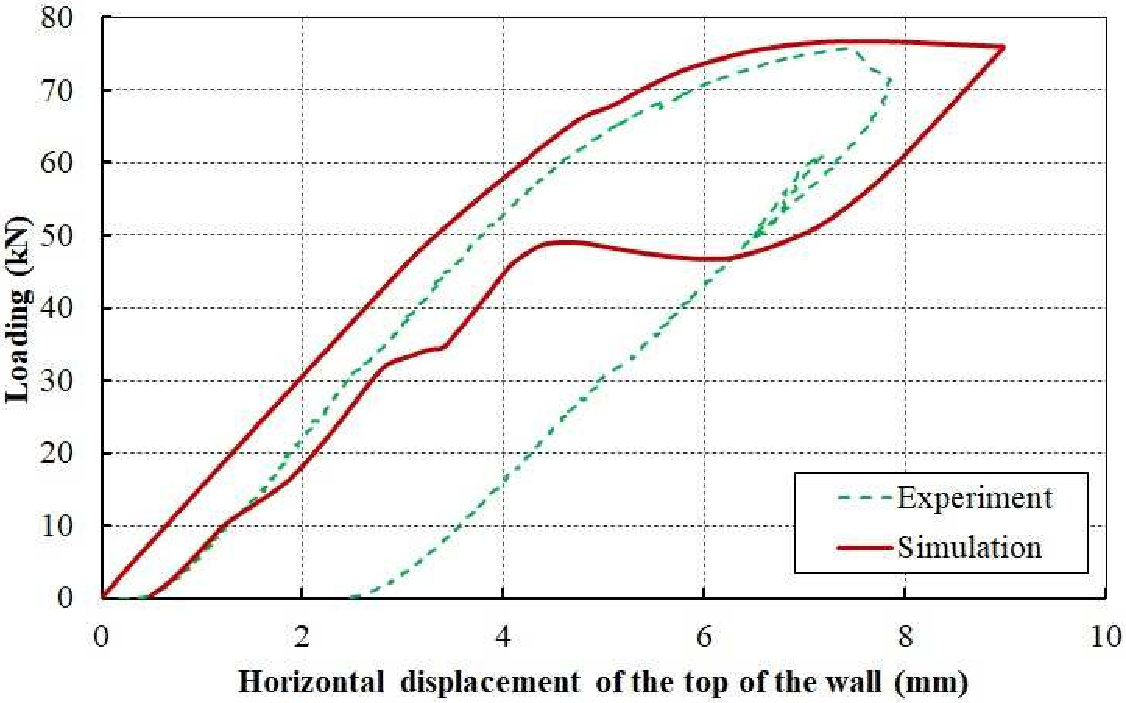

Figure 9: Force-vs-displacement curve of the URM wall during the second phase: reference case – experimental and numerical cases

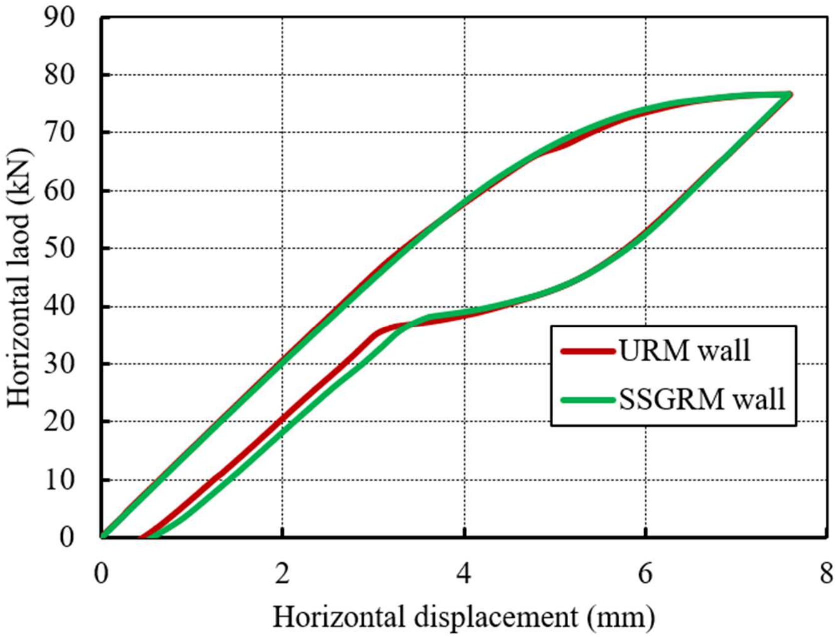

Figure 10: Force-vs-displacement curve of the URM wall and the wall repaired with SSGRM during the second phase for the damage ratio Δ = 100%.

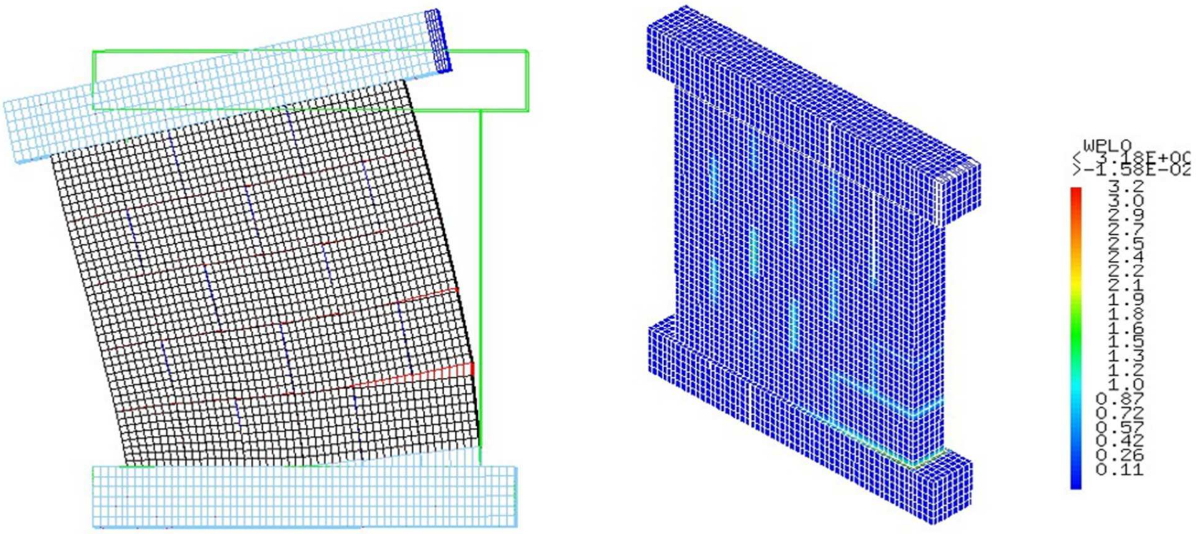

Figure 11: Deformed mesh (upscaled 40 times) of the URM wall for the maximal horizontal displacement (left) and crack width at the same time (right).

In agreement with the results of the experiment, the horizontal displacement generated during the first phase corresponds to a higher value than the one reached for peak strength. This is higher than the cases presented in [7], in which values less than or equal to 100% of the peak strengths were applied. This may result in an excess of masonry damage that could decrease the apparent efficiency of the repair solution. Therefore, it was chosen to compute phase 2 again, but for maximal horizontal displacements corresponding to the peak value of lateral strength. Let the ratio Δ denote the percentage of the maximal load applied compared with the lateral strength. In this way, the value of Δ is equal to 100%. Here, the horizontal loading of the second phase is composed of 253 displacement increments, which correspond to a maximal displacement of 7.59 mm. Then, the release of the lateral load is obtained with 252 steps of negative displacement.

The third loading phase of the repaired wall is considered next. The hydration advancement ζ is set to 1.0, at the very beginning of the reloading phase. Here, the horizontal loading starts from the residual displacement of phase 2. The aim is to evaluate the gain of strength afforded by the SSGRM, so that no release of the displacement was simulated hereafter. The force-vs-displacement curve of this phase is presented in Figure 12. This curve is expressed by considering that the lateral displacement at the beginning of phase 2 corresponds to a new origin. The load-vs-displacement relationship shows that the behaviour is almost linear until 70 kN. The initial stiffness is equal to 19.8 kN/mm, which is close to the experimental value. Then the load increases until a peak value of 97.6 kN, for a displacement of 8.29 mm. This corresponds to a strength gain of 27%. This value is even higher than the 83 kN obtained in the experiment, for which the wall was repaired along the main cracks only.

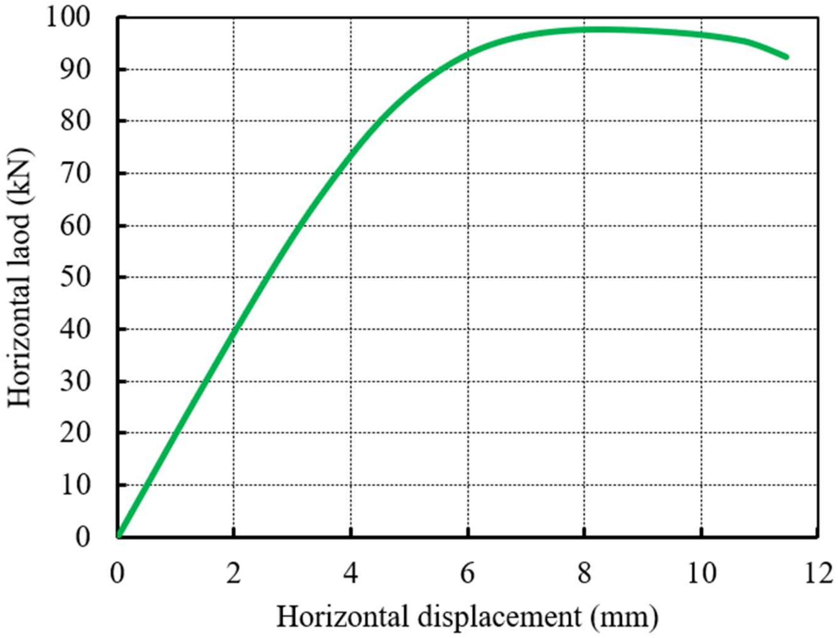

Figure 12 : Force-vs-displacement curve of the SSGRM wall during the third phase

Figure 13 shows the crack openings obtained in the repaired wall using the FE model. The results indicate that the wall failure is mainly due to crack generation along the base joint, while the repair material seems to be undamaged during the loading. This finding is very similar to the experimental case, for which the SSGRM underwent little damage. No compression damage of the SSGRM was noticed, as expected by the compression strength chosen in section 4.3. Considering the masonry on the right part of Figure 13, it appears that the crack width was negligible inside the masonry, compared with that of the base joint. Even if the masonry joints were strongly damaged during the first phase, the repair material preserved the homogeneity of the masonry. Similar results were found for ratios Δ ranging from 70% to 100%: The crack of the bottom joint is the first main failure to occur in each case, so that the failure propagates inside this joint until the maximal strength is reached. Strength gain is independent of the ratio Δ. Finally, the efficiency of the SSGRM solution is not clearly assessed in the present case, as the flexural failure does not allow an obvious test to be imposed on it.

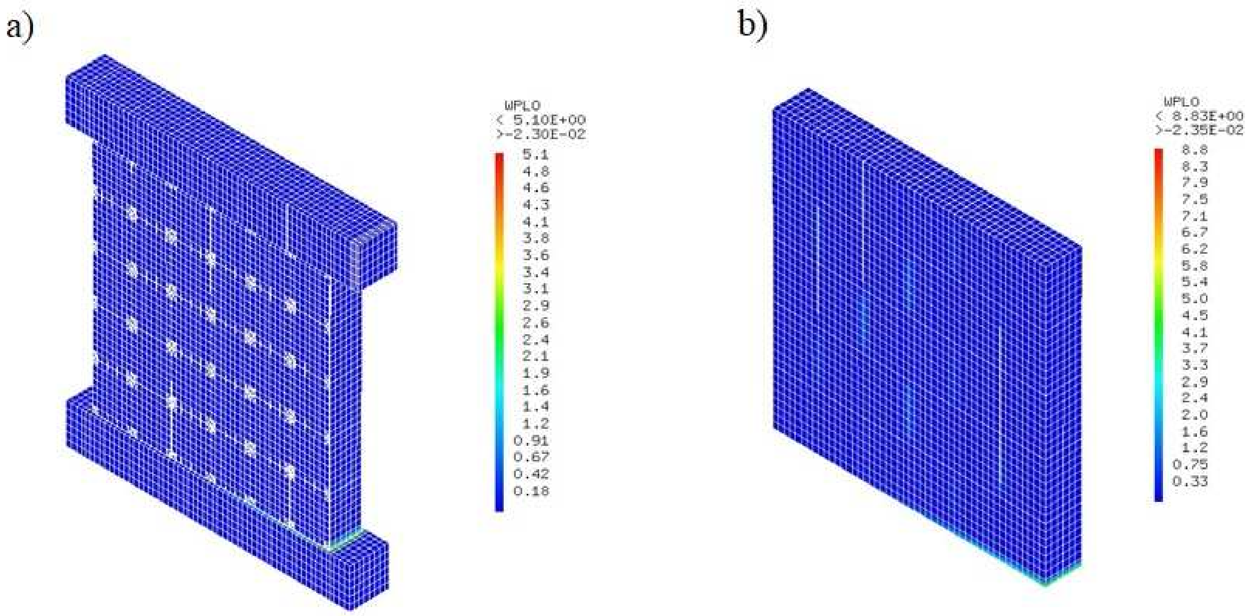

Figure 13: a) Cracks opening on the SSGRM surface for the maximal horizontal displacement and b) crack width of the sole masonry at the same time.

4.5 Sensitivity study

Having established the accuracy of the finite-element method in predicting the load-carrying capacity and behaviour of masonry walls, the FE model was used to perform a sensitivity analysis aimed at individuating the main model parameters influencing the overall behaviour and load-carrying capacity of the push-over test specimens. Here, the study focuses on the main parameters that may influence the behaviour of the URM wall and for which scarce experimental data are available. Several sets of simulations were conducted with various material properties to determine the parameters that can affect the lateral stiffness, the lateral strength, and the crack pattern of the URM wall. In each set, only one parameter was varied at a time and the remaining parameters were maintained constant. Concerning the elastic properties, the Young modulus of the bricks was considered first. In order to be coherent with the original case and as the thicknesses of the vertical joints prevent them from playing a major role in the lateral stiffness of the wall, Young's modulus of the vertical joints was set to the same value as for bricks. Then nonlinearity of the force–displacement curve is affected by the tensile fracture energy of the horizontal joints, among other parameters. Also, shear failure, which affects the wall strength, is linked to the tension and compression strengths of the horizontal joints. The effects of these parameters (tensile and compressive strengths and tensile fracture energy) were studied. The influence of the tensile strength of the base joint was also addressed. As shown in [58], the compression parameters may affect the masonry behaviour. Thus, the effects of the compression strength, the characteristic strain, the

Drucker-Prager coefficient and the dilatancy coefficient of the horizontal joints were also addressed here. Finally, the Young's modulus of the horizontal joints was in turn varied.

Each of the parameters considered was varied separately and defined close to their respective value for the original analysis (Table 1). As in the study of [58], a variation factor of 1.25 is applied to the original parameters such as Young's modulus, strengths, fracture energy. Dividing the original value by a factor 1.25 allows on to define the "conservative value" used for the parametric study. At the same time, multiplying the original value by 1.25 defines the "amplified value". The corresponding values are summarized in Table 2. For the last three parameters of Table 2, more significant variations were considered. Indeed, it is assumed that a close estimation of these parameters is quite difficult, because much less experimental data are available. Other parameters may play a significant role in the global behaviour too, but for the sake of simplicity, they were not included in the parametric study of the current work.

Table 2 : Parameters used for the sensitivity analysis

	Materials considered	Conservative value	Amplified value
Young's modulus E_B (MPa)	Brick	480	750
Tensile strength $R_{T,BJ}$ (MPa)	Base joint	0.4	0.625
Fracture energy in tension $G_{FT,HJ}$ (MJ/m²)	Horizontal joint	$0.8 \times \varepsilon_t \times R_t$	$1.25 \times \varepsilon_t \times R_t$
Tensile strength $R_{T,HJ}$ (MPa)	Horizontal joint	0.12	0.1875
Compression strength $R_{C,HJ}$ (MPa)	Horizontal joint	8	12.5
Characteristic strain $\varepsilon_{k;s,HJ}$ (-)	Horizontal joint	10^{-8}	10^{-3}
Drucker Prager coefficient δ_{JH} (-)	Horizontal joint	0.5	1.5
Dilatancy β_{JH} (-)	Horizontal joint	10^{-5}	0.1
Young's modulus E_{HJ} (MPa)	Horizontal joint	4000	6250

The analysis was repeated for the different material properties according to Table 2. The main results in terms of load-displacement diagrams are shown in Figure 14. In all the analysis, there were no changes in the failure mode discussed above and illustrated in Figure 11. The failure starts by an horizontal tensile crack that develops at the bottom of the wall at an early loading stage, followed by a diagonal stepped crack that leads to collapse. Let us define the difference Δ_{RC} to the reference case RC, in percent:

$$\Delta_{RC} = 100 \frac{|CV - AV|}{RC}$$

where CV, AV and RC denote the maximal strength reached with the conservative value, amplified value and original case.

It was observed, from the results obtained, that the Young's modulus of the brick has a significant influence on the initial stiffness and the lateral strength of the URM wall, as shown in Figure 14(a) and Table 3. However, the failure mechanisms are not affected by this variation. The influence of the

Young modulus of bricks is very significant and critical for the analysis. This can be explained by the role of this parameter that influences numerous aspects of the constitutive law.

It was also found that, within the limits established, the results are practically insensitive to the tensile strength, tensile fracture energy of horizontal–bed and intermediates joints, as shown in Figure 14(b-e). These findings are already highlighted in [58]. Contrary to the aforementioned study, Figure 14(f-h) indicates that the results are almost insensitive to the compression parameters such as the compression strength, characteristic strain, Drucker-Prager coefficient or dilatancy coefficient. This can be explained by the parameters set of Table 1, in which one of the parameters may neutralize the effect of several parameters. On the other hand, this is interesting for masonry structures because the experimental data available about these parameters are scarce and limited. Finally, the initial stiffness is almost unsensitive to the Young's modulus of the horizontal joints E_{HJ}, as shown in Figure 14(i). However, the post-peak behaviour is more affected by this variation.

These last results show that the model is consistent with the literature. However, prior to generalizing the findings, a thorough examination of key parameters and further investigations to establish the effect of other aspects such as the geometry of the wall (aspect ratio (H/L)) or the pre-compression load are required.

Table 3 : Results of the sensitivity analysis

Parameter	E_B	$R_{T,BJ}$	$G_{FT,HJ}$	$R_{T,HJ}$	$R_{C,HJ}$	$\varepsilon_{k;s,HJ}$	δ_{JH}	β_{JH}	E_{HJ}
Conservative value CV	73.46	76.68	76.66	76.61	76.67	76,63	76,66	76,64	75.98
Amplified value AV	80.04	76.73	76.67	76.77	76.67	76.70	76,72	76,70	77.9
Difference to reference case (%)	8.6	0.07	0,01	0,21	0	0.09	0.08	0,08	2.5

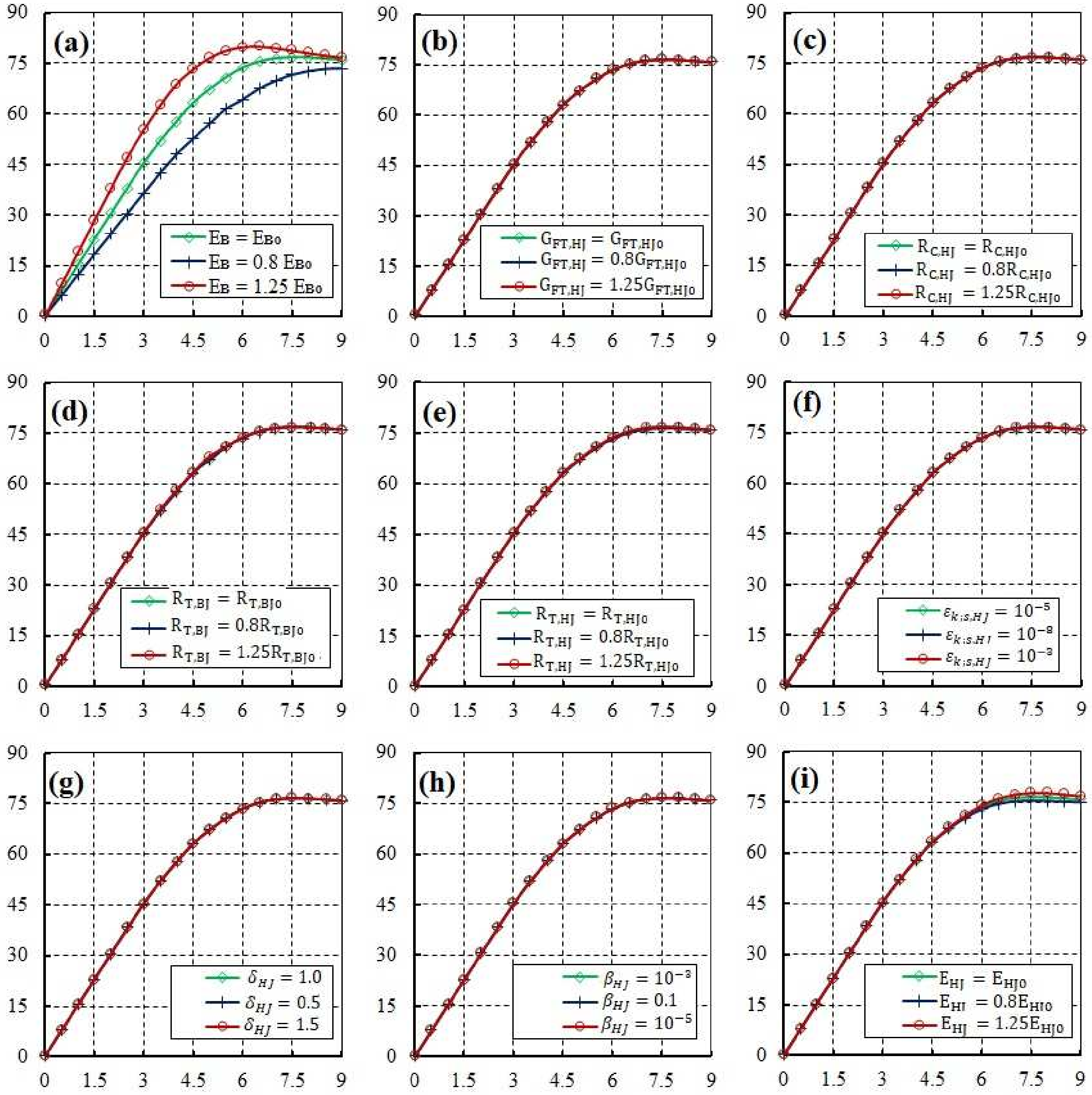

Figure 14 : Influence of the material parameters on the force-displacement diagram for masonry shear wall. (a) Young modulus of brick, (b) Tensile fracture energy of horizontal joints, (c) compressive strength of horizontal joints, (d) Tensile strength of the horizontal joint between wall and concrete beams, (e) tensile strength of horizontal joints, (f, g, h) parameters $\varepsilon_{k;s}, \beta$ and δ of horizontal joints, and (i) Young modulus of horizontal joints.

4.6 Repair efficiency of a partially damaged URM wall

Another configuration is required in order to assess the gain afforded by the repair solution. Let us consider that the failure of the two joints between the bricks and the beams is prevented. A high value of 1000 MPa was affected to the tensile strength but also to the compression strength for the base joints, so that both their tensile and shear failures are avoided. As a result, the load–displacement relationship of the second phase of the loading was modified and the curve of the horizontal displacement vs the horizontal loading is presented in Figure 15-a. The lateral strength of the wall is increased to 90.9 kN for a lateral displacement equal to 8.37 mm. This load then decreases to 84 kN for the maximal imposed displacement of 12 mm. Except for the bottom joint, the cracks occurring in the former configuration are still present; however, the masonry exhibits a staircase crack along the diagonal, as shown in Figure 15-b. This ensures that the SSGRM is tested during the third phase. In the following, it was proposed to assess its efficiency for several degrees of wall damage. According to the maximal strength established earlier, several values of the ratios Δ are presented in Table 4. The corresponding curves of the third phase of loading are presented in Figure 16 along with the maximal strength reached during this phase and the corresponding horizontal displacement in Table 4. The peak strength is approximately 150 kN, which corresponds to an increase of 66%, compared with the unreinforced wall. It is also observed that the maximal strength afforded by the repair decreases slightly with the increase in the ratio Δ. Nevertheless, theses curves are very similar for all cases. The inspection of numerical results for the case of Δ = 70% and Δ = 100% is presented in Figure 17. For the case of Δ = 70%, the maximal displacement in the phase 2 led to the opening of the vertical joints only. The first peak in phase 3 then arises for a horizontal load of 150.3 kN and for a displacement of 14.17 mm. This corresponds to the crack generation of the horizontal joint located just above the right brick of the bottom row. Then, after an initial decrease to 139.6 kN, the strength rises again but to a lower value of 142.1 kN. The corresponding displacement is 15.61 mm and the new strength reduction is due to the generation of a vertical crack in the left area of the masonry which propagates from the bottom row to the fourth row. At the maximal displacement in phase 3, this crack propagates more and more while the appearance of new vertical cracks in the same area is also noticed. For the case of Δ = 100%, besides the opening of the vertical joints, a staircase crack develops between the two first rows during phase 2. The first peak in phase 3 arises for a horizontal load of 140.9 kN, which is almost 10 kN less than the value observed with Δ = 70%. The corresponding displacement is 12.64 mm and this peak is due to the generation of a staircase crack along the long diagonal. Then, the decrease in load is accompanied by several peaks, which correspond to the generation of vertical cracks in the left part of the masonry. At the maximal displacement in phase 3, this crack propagates more and more while the appearance of new vertical cracks in the same area is also noticed. Finally, no damage in compression was noticed for the SSGRM in any simulation, as expected by the choice of compression strength stated in section 4.3. No crack is visible at any stage of the simulations on the SSGRM surface, but a closer inspection indicates that cracks have started to propagate at the SSGRM–brick interface.

With the last simulations, the SSRGM was not tested to its maximal strength. Despite this, its efficiency to reinforce the masonry was highlighted, with a gain of almost 60% in all cases. The strength loss between the cases of Δ = 70% and Δ = 100% is worth noting, because it represents only 10 kN of the 60 kN gained, compared with the URM configuration.

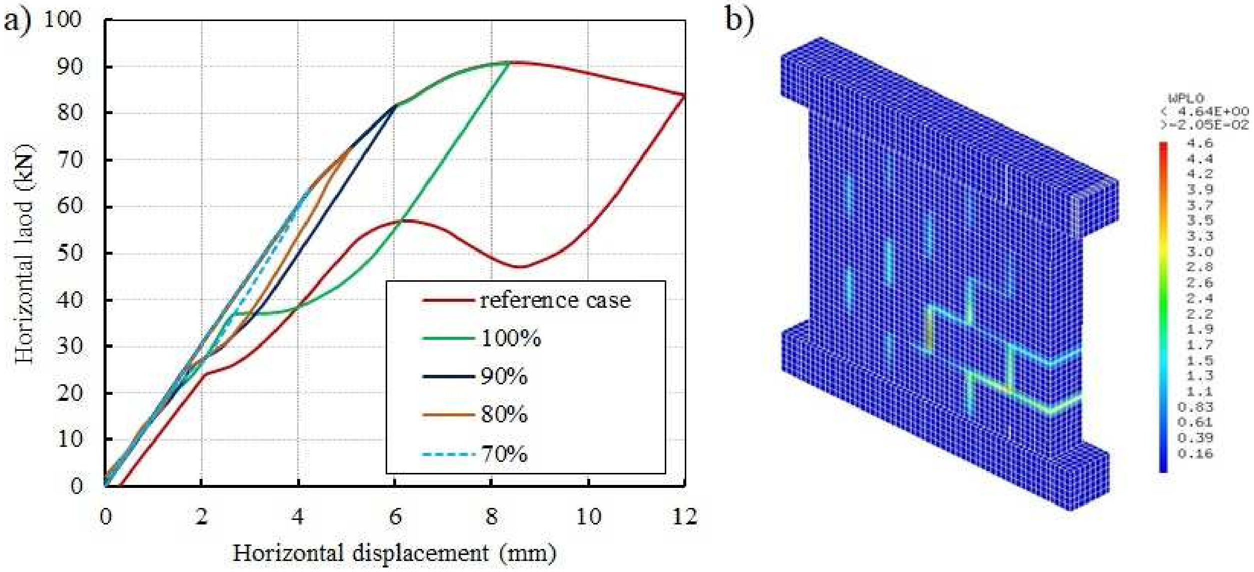

Figure 15: a) Force-vs-displacement curve of the second phase of the modified model for several values of the ratio Δ and b) crack width for the maximal displacement of 12 mm.

Table 4: Summary of the numerical results obtained for the different degrees of damage to the wall

Ratio Δ	70%	80%	90%	100%
Horizontal loading (kN)	63,8	72,6	81,8	90,9
Horizontal displacement (mm)	4,24	5,08	6,03	8,37
Maximal strength of phase 3 (kN)	150,3	149,5	145,4	140,9
Corresponding displacement (mm)	14,17	13,87	13,55	12,64

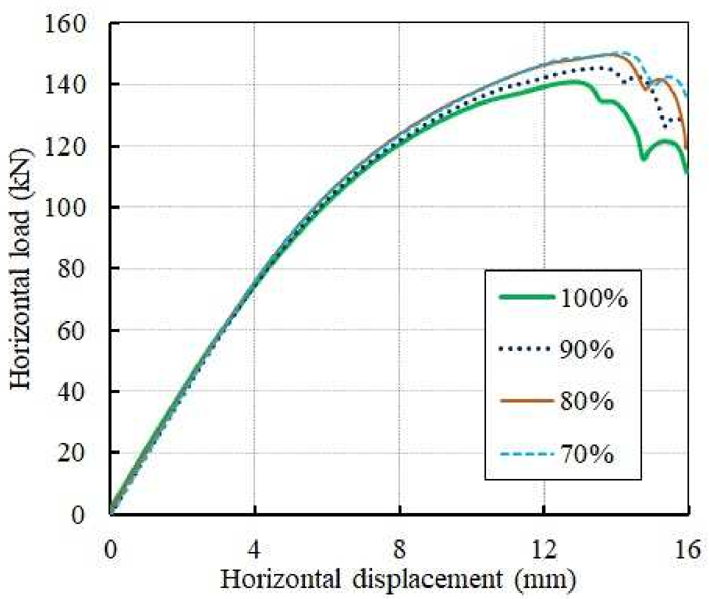

Figure 16: Force-vs-displacement curve of phase 3 of the modified model for several values of the ratio Δ.

	Crack openings at the maximum lateral displacement		
	URM without SSGRM Composite (inactivated Elements) (phase 2)	Wall with SSRGRM Composite (phase 3)	Repaired Masonry (the SSRGRM Element were omitted) (phase 3)
Δ = 70%	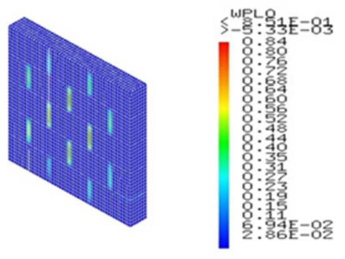	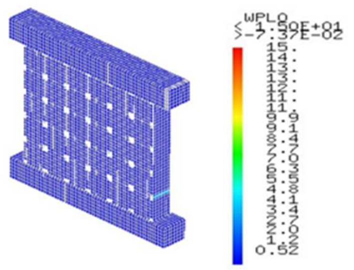	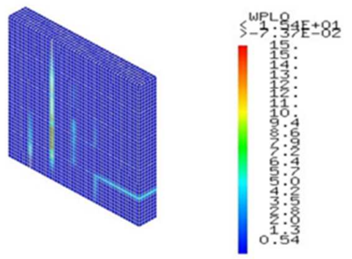
Δ = 100%	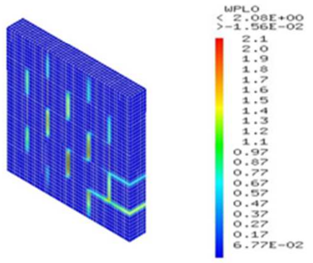	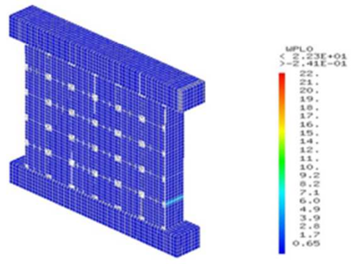	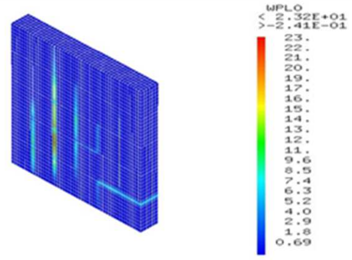

Figure 17 : Cracks opening for the 70% (top) and 100% (bottom) ratios at different times: on the masonry surface for the maximal displacement in phase 2 (left), on the SSGRM surface for the maximal displacement in phase 3 (middle), on the masonry surface for the maximal displacement in phase 3 (middle).

5 Conclusion

This work focuses on an exploratory study of an innovative textile-reinforced mortar dedicated to masonry repair. This comprises characterization tests, damage and repair of an experimental wall and finally the numerical modelling of the previously cited experiments. On the basis of this work, several statements can be made:

1. A Stainless-Steel Grid-Reinforced Mortar solution was proposed for the repair of masonry. The ductile nature of the stainless-steel grid afforded the possibility to maintain the strength of the composite, even for very high strain ratios. Its application as a seam on the masonry ensures the possibility to recover the wall strength against a lateral loading. Moreover, an interesting gain of strength was also noticed.
2. A micro-modelling finite-element approach of the experiment on the wall was proposed. Here, mortar joints are not modelled with interface elements, but with solid element. This allows one to model joints and repair material in the same model. The behaviour of the composite was homogenized and simplified, but its tensile behaviour and, its bond strength on the brick were incorporated.
3. The constitutive law retained is usually dedicated to the modelling of concrete structures. Here, it was applied to the masonry elements (bricks, mortar joints, dry joints) but also for the repair material. For some of the parameters, default values were used to compensate for the requirement to define them in other experiments. This is the case for the mortar joints for which shear tests on triplets could have been undertaken. Despite this, most of the features observed during the experimental damage phase were reproduced: the initial stiffness, the maximal strength and its corresponding horizontal displacement, the damaged area. However, the failure inside the central brick of the bottom row could not be reproduced, nor the strength loss observed during the post-peak area.
4. The experimental damage phase of the wall, before repair application, was modelled correctly: Finite-elements representing the repair material were activated only after the damage phase. This is a clear improvement to the modelling of retrofitting configurations proposed in the literature. The simulation of the repaired wall presented a gain of strength that is even higher than the experimental case. This finding is consistent, as the repair was applied locally during the experiment, while the whole covering of both sides was chosen numerically. Even if the results were coherent, the evaluation of the composite was not efficient because of the flexural failure of the wall.
5. A final configuration was tested, in which failure of the joints between the bricks and the concrete beams was prevented. In this way, the crack generation is located in the masonry part and the efficiency of the SSGRM can be assessed. A gain of almost 60% emerged from the different damage configurations tested. The strength of the repair masonry is almost non-dependent on the state of the damaged masonry. The cracks propagate in the interface of the SSGRM, but do not extend to the SSGRM core. This shows that the repair material still has a mobilizable strength, which could be assessed in the case of more resistant masonry.

An additional experimental campaign is required to confirm the SSGRM capacity after the standards. The same applies for the experiments at wall scale, for which several specimens involving reproducibility, the effects of the wall slenderness, the vertical loading and finally the repair configurations could be considered. Characterization tests of the different joints would also be useful, in order to apply the appropriate parameters to the numerical model. Nevertheless, the modelling of successive phases of damage and of repair yielded good results and characterizes the main innovation of the current work. The extension of this method to the field of repaired concrete structures may represent a good opportunity.

6 References

[1] CEN. Eurocode 6: Design of masonry structures - Part 1-1: General rules for reinforced and unreinforced masonry structures. 2005.

[2] Eurocode C. 8: Design of structures for earthquake resistance—Part 1: General rules, seismic actions and rules for buildings (EN 1998-1: 2004). Eur Comm Norm Brussels 2004.

[3] Bournas DA. Concurrent seismic and energy retrofitting of RC and masonry building envelopes using inorganic textile-based composites combined with insulation materials: A new concept. Compos Part B Eng 2018;148:166–79. https://doi.org/10.1016/j.compositesb.2018.04.002.

[4] Mistretta F, Stochino F, Sassu M. Structural and thermal retrofitting of masonry walls: An integrated cost-analysis approach for the Italian context. Build Environ 2019;155:127–36. https://doi.org/10.1016/j.buildenv.2019.03.033.

[5] Triantafillou TC, Karlos K, Kefalou K, Argyropoulou E. An innovative structural and energy retrofitting system for URM walls using textile reinforced mortars combined with thermal insulation: Mechanical and fire behavior. Constr Build Mater 2017;133:1–13. https://doi.org/10.1016/j.conbuildmat.2016.12.032.

[6] Eymard M. Analyse du comportement mécanique de l'interface entre un enduit d'isolation thermique innovant et son support structurel 2014.

[7] Santa-Maria H, Alcaino P. Repair of in-plane shear damaged masonry walls with external FRP. Constr Build Mater 2011;25:1172–80. https://doi.org/10.1016/j.conbuildmat.2010.09.030.

[8] Mosallam A, Banerjee S. Enhancement in in-plane shear capacity of unreinforced masonry (URM) walls strengthened with fiber reinforced polymer composites. Compos Part B Eng 2011;42:1657–70. https://doi.org/10.1016/j.compositesb.2011.03.015.

[9] Konthesingha KMC, Masia MJ, Petersen RB, Mojsilovic N, Simundic G, Page AW. Static cyclic in-plane shear response of damaged masonry walls retrofitted with NSM FRP strips - An experimental evaluation. Eng Struct 2013;50:126–36. https://doi.org/10.1016/j.engstruct.2012.10.026.

[10] Anania L, Badala A, Costa S, D'Agata G, Giacquinta C. Experimental investigation of masonry calcareous walls repaired and strengthened by C-FRP. Proc 13th East Asia-Pacific Conf Struct Eng Constr EASEC 2013 2013.

[11] Marcari G, Manfredi G, Prota A, Pecce M. In-plane shear performance of masonry panels strengthened with FRP. Compos Part B Eng 2007;38:887–901. https://doi.org/10.1016/j.compositesb.2006.11.004.

[12] Babatunde SA. Review of strengthening techniques for masonry using fiber reinforced polymers. Compos Struct 2017;161:246–55. https://doi.org/10.1016/j.compstruct.2016.10.132.

[13] Corradi M, Di Schino A, Borri A, Rufini R. A review of the use of stainless steel for masonry repair and reinforcement. Constr Build Mater 2018;181:335–46. https://doi.org/10.1016/j.conbuildmat.2018.06.034.

[14] Bui TL, Si Larbi A, Reboul N, Ferrier E. Shear behaviour of masonry walls strengthened by external bonded FRP and TRC. Compos Struct 2015;132:923–32. https://doi.org/10.1016/j.compstruct.2015.06.057.

[15] Babaeidarabad S, Arboleda D, Loreto G, Nanni A. Shear strengthening of un-reinforced concrete masonry walls with fabric-reinforced-cementitious-matrix. Constr Build Mater 2014;65:243–53. https://doi.org/10.1016/j.conbuildmat.2014.04.116.

[16] Basili M, Vestroni F, Marcari G. Brick masonry panels strengthened with textile reinforced mortar: experimentation and numerical analysis. Constr Build Mater 2019;227:117061. https://doi.org/10.1016/j.conbuildmat.2019.117061.

[17] Kouris LAS, Triantafillou TC. State-of-the-art on strengthening of masonry structures with textile reinforced mortar (TRM). Constr Build Mater 2018;188:1221–33. https://doi.org/10.1016/j.conbuildmat.2018.08.039.

[18] Carozzi FG, Poggi C, Bertolesi E, Milani G. Ancient masonry arches and vaults strengthened with TRM, SRG and FRP composites: Experimental evaluation. Compos Struct 2018;187:466–80. https://doi.org/10.1016/j.compstruct.2017.12.075.

[19] De Santis S, De Felice G. Tensile behaviour of mortar-based composites for externally bonded reinforcement systems. Compos Part B Eng 2015;68:401–13. https://doi.org/10.1016/j.compositesb.2014.09.011.

[20] Plassiard JP, Plé O, Perrotin P. Repair of a masonry wall with an innovative ciment based composite. 9th Int Conf Fibre-Reinforced Polym Compos Civ Eng CICE 2018 2018;2018-July:130–7.

[21] Menna C, Asprone D, Durante M, Zinno A, Balsamo A, Prota A. Structural behaviour of masonry panels strengthened with an innovative hemp fibre composite grid. Constr Build Mater 2015;100:111–21. https://doi.org/10.1016/j.conbuildmat.2015.09.051.

[22] Mustafaraj E, Yardim Y. Retrofitting damaged unreinforced masonry using external shear strengthening techniques. J Build Eng 2019;26:100913. https://doi.org/10.1016/j.jobe.2019.100913.

[23] Ghobadi MS, Jazany RA, Farshchi H. In situ repair technique of infill masonry walls in steel frames damaged after an earthquake. Eng Struct 2019;178:665–79. https://doi.org/10.1016/j.engstruct.2018.10.022.

[24] Messali F, Metelli G, Plizzari G. Experimental results on the retrofitting of hollow brick masonry walls with reinforced high performance mortar coatings. Constr Build Mater 2017;141:619–30. https://doi.org/10.1016/j.conbuildmat.2017.03.112.

[25] De Santis S, de Felice G. Steel reinforced grout systems for the strengthening of masonry structures. Compos Struct 2015;134:533–48. https://doi.org/10.1016/j.compstruct.2015.08.094.

[26] Asteris PG, Cotsovos DM, Chrysostomou CZ, Mohebkhah A, Al-Chaar GK. Mathematical micromodeling of infilled frames: State of the art. Eng Struct 2013;56:1905–21. https://doi.org/10.1016/j.engstruct.2013.08.010.

[27] D'Ambra C, Lignola GP, Prota A, Fabbrocino F, Sacco E. FRCM strengthening of clay brick walls for out of plane loads. Compos Part B Eng 2019;174:107050. https://doi.org/10.1016/j.compositesb.2019.107050.

[28] Lourenço PB. Computational strategies for masonry structures. 1996. https://doi.org/ISBN 90-407-1221-2.

[29] Bertolesi E, Milani G, Poggi C. Simple holonomic homogenization model for the non-linear static analysis of in-plane loaded masonry walls strengthened with FRCM composites. Compos Struct 2016;158:291–307. https://doi.org/10.1016/j.compstruct.2016.09.027.

[30] D'Altri AM, de Miranda S, Castellazzi G, Sarhosis V. A 3D detailed micro-model for the in-plane and out-of-plane numerical analysis of masonry panels. Comput Struct 2018;206:18–30. https://doi.org/10.1016/j.compstruc.2018.06.007.

[31] Pourfalah S, Cotsovos DM, Suryanto B. Modelling the out-of-plane behaviour of masonry walls retrofitted with engineered cementitious composites. Comput Struct 2018;201:58–79. https://doi.org/10.1016/j.compstruc.2018.02.004.

[32] Nazir S, Dhanasekar M. A non-linear interface element model for thin layer high adhesive mortared masonry. Comput Struct 2014;144:23–39. https://doi.org/10.1016/j.compstruc.2014.07.023.

[33] Grande E, Milani G. Interface modeling approach for the study of the bond behavior of FRCM strengthening systems. Compos Part B Eng 2018;141:221–33. https://doi.org/10.1016/j.compositesb.2017.12.052.

[34] Milani G, Grande E. Simple bisection procedure in quickly convergent explicit ODE solver to numerically analyze FRCM strengthening systems. Compos Part B Eng 2020;199:108322. https://doi.org/10.1016/j.compositesb.2020.108322.

[35] Grande E, Imbimbo M, Sacco E. Numerical investigation on the bond behavior of FRCM strengthening systems. Compos Part B Eng 2018;145:240–51. https://doi.org/10.1016/j.compositesb.2018.03.010.

[36] Sellier A, Casaux-Ginestet G, Buffo-Lacarrière L, Bourbon X. Orthotropic damage coupled with localized crack reclosure processing. Part I: Constitutive laws. Eng Fract Mech 2013;97:148–67. https://doi.org/10.1016/j.engfracmech.2012.10.012.

[37] CEA. CAST3M17 2017. n.d. http://www-cast3m.cea.fr.

[38] Committee RT. Recommendation of RILEM TC 232-TDT : test methods and design of textile

reinforced concrete 2016:4923–7. https://doi.org/10.1617/s11527-016-0839-z.

[39] Felice G De, Antonietta M, Carmelo A, Ceroni F, Santis S De, Garbin E, et al. Recommendation of RILEM Technical Committee 250-CSM : Test method for Textile Reinforced Mortar to substrate bond characterization 2018:1–9. https://doi.org/10.1617/s11527-018-1216-x.

[40] Contamine R., Plassiard J.-P. PP. Confrontation de composites textile-mortier (TRC) à renfort carbone ou acier pour le renforcement d'éléments de maçonnerie. 33èmes Rencontres de l'AUGC, ISABTP/UPPA, 2015, p. 1–8.

[41] Vacher P, Dumoulin S, Morestin F, Mguil-Touchal S. Bidimensional strain measurement using digital images. Proc Inst Mech Eng Part C J Mech Eng Sci 1999;213:811–7. https://doi.org/10.1243/0954406991522428.

[42] Eymard M. Analyse du comportement mécanique de l'interface entre un enduit d'isolation thermique innovant et son support structurel 2014.

[43] Papanicolaou C, Triantafillou T, Lekka M. Externally bonded grids as strengthening and seismic retrofitting materials of masonry panels. Constr Build Mater 2011;25:504–14. https://doi.org/10.1016/j.conbuildmat.2010.07.018.

[44] Bui T, Larbi AS, Reboul N, Ferrier E. Shear behaviour of masonry walls strengthened by external bonded FRP and TRC. Compos Struct 2015;132:923–32. https://doi.org/10.1016/j.compstruct.2015.06.057.

[45] Noor-E-Khuda S, Dhanasekar M. Masonry Walls under Combined In-Plane and Out-of-Plane Loadings. J Struct Eng (United States) 2018. https://doi.org/10.1061/(ASCE)ST.1943-541X.0001930.

[46] Scacco J, Ghiassi B, Milani G, Lourenço PB. A Fast Modeling Approach for Numerical Analysis of Unreinforced and FRCM Reinforced Masonry Walls under Out-Of-Plane Loading. Compos Part B 2019:107553. https://doi.org/10.1016/j.compositesb.2019.107553.

[47] Tarque N, Candido L, Camata G, Spacone E. Masonry infilled frame structures: State-of-the-art review of numerical modelling. Earthq Struct 2015;8:225–51. https://doi.org/10.12989/eas.2015.8.1.225.

[48] Margiacchi F, Salvatori L, Orlando M, De Stefano M, Spinelli P. Seismic response of masonry-infilled steel frames via multi-scale finite-element analyses. Bull Earthq Eng 2016;14:3529–46. https://doi.org/10.1007/s10518-016-0012-7.

[49] Milani G, Valente M, Fagone M, Rotunno T, Alessandri C. Advanced non-linear numerical modeling of masonry groin vaults of major historical importance: St John Hospital case study in Jerusalem. Eng Struct 2019;194:458–76. https://doi.org/10.1016/j.engstruct.2019.05.021.

[50] Conde B, Ramos LF, Oliveira D V., Riveiro B, Solla M. Structural assessment of masonry arch bridges by combination of non-destructive testing techniques and three-dimensional numerical modelling: Application to Vilanova bridge. Eng Struct 2017;148:621–38. https://doi.org/10.1016/j.engstruct.2017.07.011.

[51] Belghiat C, Messabhia A, Plassiard JP, Guenfoud M, Plé O, Perrotin P. Experimental study of double-panel confined masonry walls under lateral loading. J Build Eng 2018. https://doi.org/10.1016/j.jobe.2018.09.001.

[52] Wang X, Ghiassi B, Oliveira D V, Lam CC. Modelling the nonlinear behaviour of masonry walls strengthened with textile reinforced mortars. Eng Struct 2017;134:11–24. https://doi.org/10.1016/j.engstruct.2016.12.029.

[53] Scacco J, Ghiassi B, Milani G, Lourenço PB. A fast modeling approach for numerical analysis of unreinforced and FRCM reinforced masonry walls under out-of-plane loading. Compos Part B Eng 2020;180:107553. https://doi.org/10.1016/j.compositesb.2019.107553.

[54] Sellier A, Casaux-Ginestet G, Buffo-Lacarrière L, Bourbon X. Orthotropic damage coupled with localized crack reclosure processing. Part I: Constitutive laws. Eng Fract Mech 2013. https://doi.org/10.1016/j.engfracmech.2012.10.012.

[55] Sellier A, Multon S, Buffo-Lacarrière L, Vidal T, Bourbon X, Camps G. Concrete creep modelling for structural applications: Non-linearity, multi-axiality, hydration, temperature and drying effects. Cem Concr Res 2016;79:301–15. https://doi.org/10.1016/j.cemconres.2015.10.001.

[56] Sellier A, Casaux-Ginestet G, Buffo-Lacarrière L, Bourbon X. Orthotropic damage coupled with localized crack reclosure processing Part II: Applications. Eng Fract Mech 2013. https://doi.org/10.1016/j.engfracmech.2012.10.016.

[57] Hillerborg A, Modéer M, Petersson PE. Analysis of crack formation and crack growth in concrete by means of fracture mechanics and finite elements. Cem Concr Res 1976. https://doi.org/10.1016/0008-8846(76)90007-7.

[58] Lourenço PB. Sensitivity Analysis of Masonry Structures. 8th Int Symp Can Mason 1998:563–74.

7 Acknowledgments

The authors would like to acknowledge the LOCIE laboratory and the Savoie Mont Blanc University (USMB) for their financial supports. The cement matrix and wall construction were supplied by the companies Parex Lanko and Wienerberger, respectively. Major assistance was also provided during the experiment by Frédéric Pouxviel (3R company) in order to develop the test sequence involving the in-situ stress. Modelling the repaired wall was possible thanks to the help of Alain Sellier (Laboratory LMDC, Toulouse). Finally, the authors are grateful for the help provided by Gregory Gonon and Yoann Perrat, two students from USMB University, who helped to carry out the experimental phase.